Characterizing and Minimizing Nonlinearities Responsible for Intermodulation Distortion in High Speed and High Power Photodiodes

A Thesis
Presented to
The Academic Faculty

by

Margaret A. Fitzharris

In Partial Fulfillment
of the Requirements for the Degree
Master of Science in Electrical and Computer Engineering in the
School of Electrical and Computer Engineering

Georgia Institute of Technology
May 2016

Characterizing and Minimizing Nonlinearities Responsible for Intermodulation Distortion in High Speed and High Power Photodiodes

Approved by:

Dr. Paul D. Yoder, Advisor
School of Electrical and Computer Engineering
Georgia Institute of Technology

Dr. Benjamin D. B. Klein
School of Electrical and Computer Engineering
Georgia Institute of Technology

Dr. Shyh-Chiang Shen
School of Electrical and Computer Engineering
Georgia Institute of Technology

Date Approved: April 29, 2016

ACKNOWLEDGEMENTS

I would like to thank my advisor, Dr. Paul D. Yoder, from the Georgia Institute of Technology, for his continual guidance and assistance towards my research. I would like to thank the committee members, Dr. Benjamin D. B. Klein and Dr. Shyh-Chiang Shen, also from the Georgia Institute of Technology, for their advice. This experience has been invaluable, and I am entirely grateful.

TABLE OF CONTENTS

LIST OF TABLES

LIST OF FIGURES

LIST OF SYMBOLS

PD	photodiode
p-n PD	photodiode with p-type followed by an n-type region
p-i-n PD	photodiode with p-type, followed by an intrinsic region, followed by an *n*-type region
UTC PD	uni-traveling carrier photodiode
IP3	third-order local intercept point (IP3), or the intercept point in the third-order intermodulation distortion plot (IMD3) (electrical output power versus optical input power), where the output power at the fundamental frequency is equal to the output power at the third-order harmonic frequency
IMD3	third-order intermodulation distortion
v_{diode}	diode voltage
x_c	depletion region thickness
$E(x_b)$	the electric field at the anode side of the depletion region
v_{bi}	the built-in junction potential of the photodiode
N_D	the doping density
$n(x_b)$	the electron density at the beginning of the depletion region
v_{sat}	the saturated electron velocity
A	the cross-sectional area
E_{ph}	the energy of a photon
h	Planck's constant
f	frequency of the light
R_l	the load resistance

P_{in}	optical input power absorbed within the UTC photodiode
P_{out}	electrical output power
q	the charge of an electron
ε	the permittivity of the depleted collector
N_D^-	the doping density in the depletion region
n	the electron density generated by the optical illumination
v_A	the applied voltage to the circuit
I_{diode}	the current through the diode
ω_a, ω_b	stimulus frequency

SUMMARY

A physics-based model incorporating the UTC (uni-traveling carrier) photodiode (PD) in the limit of weak nonlinearity was used in order to characterize the effects of nonlinearity on high speed and high power photodiodes [1-7]. The combined influences of a) optical illumination, b) photocurrent, and c) interaction of the photodiode with an external circuit, were incorporated into three equations which described the phasor dynamics of the photodiode, which could be used to approximate the diode voltage (v_{diode}), the depletion region thickness (x_c), and the electric field at the beginning of the depletion region ($E(x_b)$) by the Newton-Raphson Method [8-11].

Then a frequency response plot as well as a third-order intermodulation distortion (IMD3) plot were obtained in order to evaluate the effects of nonlinearity on the photodiode [12-18]. The third-order intercept point (IP3) was determined to be approximately $27.5\ dB$, illustrating its slight nonlinearity.

For both the frequency and the IMD3 plots, it was shown that modulation bandwidth is predominantly RC-limited and that the stated assumptions were true: that the average electron transit time through the depletion region is expected to be significantly smaller than the period of the optical stimulus.

Finally, nonlinearity was minimized by compensating the heavy loading and space charge effects on junction capacitance, and a surface plot was obtained demonstrating this behavior [1-3].

CHAPTER 1
INTRODUCTION

Since its growth in popularity in the 1940s, photodiodes have been key in photonic applications [19-29]. Photodiodes have been integrated into linear systems for applications such an image sensing and ultraviolet light detection [30-32]. However, due to the recent demand for high speed and high data transfer for telecommunications, photodiodes have been more commonly used in high speed and high power applications, which can lead to nonlinearity, as well as deleterious effects, such as intermodulation distortion and bandwidth collapse [1-3]. Thus, several recent efforts have been made in order to minimize these effects. B. Troyanovsky *et al.* [33] utilized the harmonic balance method, typically used to describe nonlinearity in RF and microwave circuits, to characterize nonlinearity in semiconductor devices by developing a physics-based, analytical model for large-signal steady-state analysis which can be incorporated in wireless communication systems. A. Hastings *et al.* [34] minimized photodiode nonlinearities in *p-i-n* photodiodes by offsetting voltage-dependent responsivity effects, due to impact ionization and the Franz-Keldysh effect. H. Pan *et al.* [35] also minimized nonlinearity in an InGaAs/InP charge compensated modified uni-traveling carrier photodiode by offsetting certain bias and photocurrent to cancel out photocurrent and voltage-dependent capacitance effects. H. Pan *et al.* [36] characterized the nonlinearity in an InGaAs/InP charge compensated modified uni-traveling carrier photodiode using a two-tone setup to describe the responsivity and capacitance effects.

The objective of the proposed research will be to investigate the microscopic origins of nonlinearity leading to intermodulation distortion in high power, high speed photodiodes from a theoretical perspective[1-3]. The design will focus exclusively on the uni-traveling carrier (UTC)

photodiode (PD) [4-7], a recently developed PD whose photocurrent is only determined by electrons (with no contribution from holes). A system of nonlinear equations will be derived which describes the coupled influences of a) optical illumination, b) photocurrent, and c) interaction of the photodiode with an external circuit. Under the assumption of weak nonlinearity, these coupled equations will be formulated as a system of harmonic balance equations [33], which describe the magnitude and phase of the PD response to multiple simultaneous sinusoidal stimuli at the fundamental frequencies as well as harmonics and interharmonics of arbitrary order. The Newton-Raphson method will be used to solve these simultaneous equations iteratively [8-11]. The phasor response of the photodiode to multi-tone stimulus will be characterized by three characteristic properties of the photodiode, one macroscopic and two microscopic: diode voltage (v_{diode}), the depletion region thickness (x_c), and the electric field at the beginning of the depletion region ($E(x_b)$).

The influence of nonlinearity on intermodulation distortion and bandwidth collapse will be studied in terms of the relevant phasor harmonics of the aforementioned microscopic quantities, and the photocurrent induced through a load resistance of an external circuit. Due to the low bias levels applied to UTC PDs in telecommunications applications, nonlinear effects such as Zener tunneling, defect-assisted tunneling, and avalanche generation will be presumed negligible [1-3]. Furthermore, non-linear effects associated with extreme optical stimulation, such as optical bleaching (Burstein-Moss effect) and bandgap renormalization, are known to be insignificant at power levels typical for telecommunications applications [1-3]. As a consequence, nonlinearities considered in the work of this thesis will be limited to those associated with heavy loading and bias-dependent junction capacitance [1-3].

In the coming chapters, the origin and history of nonlinear photodiodes will be discussed; a physics-based model will be derived in order to approximate the diode voltage (v_{diode}), depletion region thickness (x_c), and the electric field at the beginning of the depletion region ($E(x_b)$); a frequency response plot as well as an IMD3 plot [12-17] will be obtained in order to evaluate the effects of nonlinearity on the photodiode response; and, finally, the causes of nonlinearity, due to heavy loading and bias-dependent junction capacitance [1-3], will be minimized.

CHAPTER 2
ORIGIN AND HISTORY OF NONLINEAR PHOTODIODES

P-n junctions grew in popularity during the 1940s [19]. This focus on *p-n* junctions later led to the development of the *p-i-n* photodiode in the late 1950s due to the growth in interest from rectifying signals to photonic applications, such as photodiodes, solar cells, and light emission. While they were growing in popularity, other types of photodiodes were also developed [19-29].

The *p-n* photodiode [19-29] consists of a *p*-type region followed by an *n*-type region.

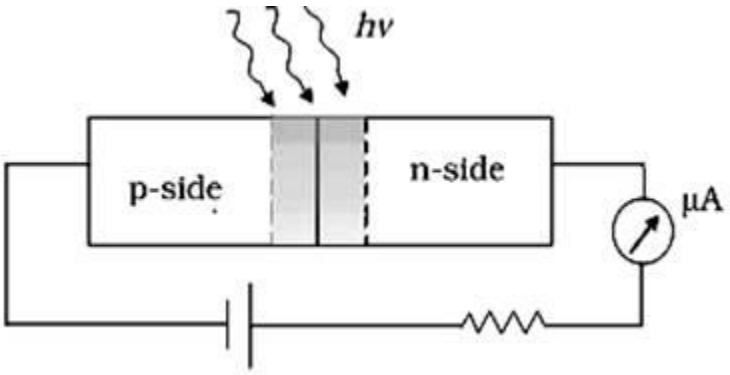

Figure 1: Band diagram of a *p-n* PD under low optical illumination [27].

When a photon with sufficient energy, greater than the bandgap energy, is absorbed within the depletion region, a valence electron is promoted across the bandgap to the conduction band, leaving behind a hole in the valence band [19-29]. The electric field within the junction causes the holes to drift to the *p*-side depletion region boundary and the electrons to drift to the *n*-side boundary. During the time of their drift within the depletion region, they may both induce current in an external circuit, such as the one shown in Figure 1. Upon reaching their respective

depletion region boundaries, the electron and hole are collected nearly instantaneously. Because each photon generates one electron-hole pair, low-frequency photocurrent is proportional to the power associated with the absorbed optical signal [19-29]. Photons may also be absorbed within the quasi-neutral regions on either side of the depletion region, but only those electron-hole pairs photogenerated within approximately one diffusion length of the boundaries may contribute effectively to the photocurrent [19-29].

The *p-i-n* photodiode [19-29] adds an intrinsic (undoped) region between the *p* and *n*-type regions in the *p-n* photodiode.

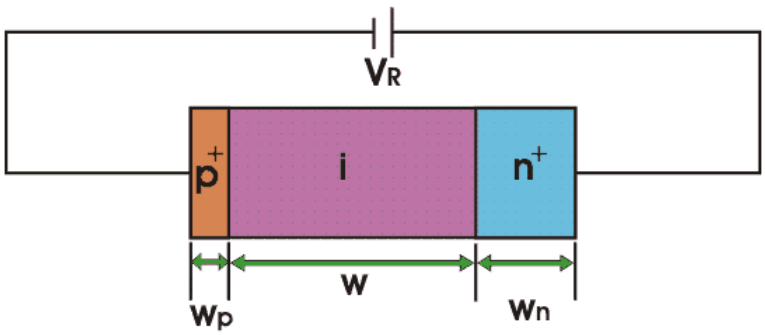

Figure 2: Band diagram of a *p-i-n* PD under low optical illumination [28].

This intrinsic region is fully depleted at typical applied bias levels, allowing for higher quantum efficiency (due to the increased volume in which photogenerated carriers contribute to the photocurrent) and lower capacitance than the *p-n* junction diode [19-29].

P-i-n photodiodes [19-29] are the most commonly used photodiode today. Like *p-n* photodiodes, they have a very simple epitaxial structure and can be grown and fabricated for a wide range of applications. They are used in audio CD players, DVD players, computer CD drives, as well as optical communication systems and nuclear radiation detectors [19-29].

A Schottky diode [19-29] consists of a semiconductor material bounded by a unilateral junction and an ideal, non-rectifying Ohmic bilateral contact, with no potential across it.

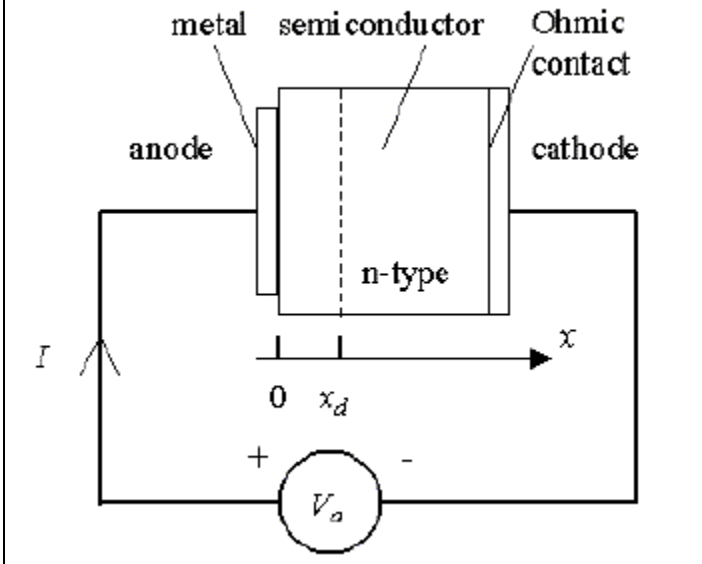

Figure 3: Band diagram and equivalent circuit model of a Schottky PD under low optical illumination [29].

In the absence of optical illumination, when a reverse-bias is applied across the diode, only a small leakage current flows from the metal contact to the Ohmic contact [19-29].

A Schottky photodiode [19-29] exhibits high speed and long wavelength detection capability, and can be used as a photodiode. It is used as an image sensing photodetector in charge coupled devices (CCDs). It can also be used in focal plane arrays, where it is integrated with the CCD transfer gate into a single chip, which serves as a shift register to transfer the data from a Schottky diode array [19-29].

As an example of the use of PDs in commercial applications, *p-n* junction photodetectors may be used in image sensor structures [30] designed to improve CCDs, or charge coupled

devices, by using a CMOS photodiode image sensor. This design consists of two *p*-*n* photodiodes in the photo-sensing region of the substrate, where the *n*-type terminal is connected to the source/drain region of the first transistor, and the contact, coupled with the second *p*-*n* photodiode, is connected to the gate of the second transistor.

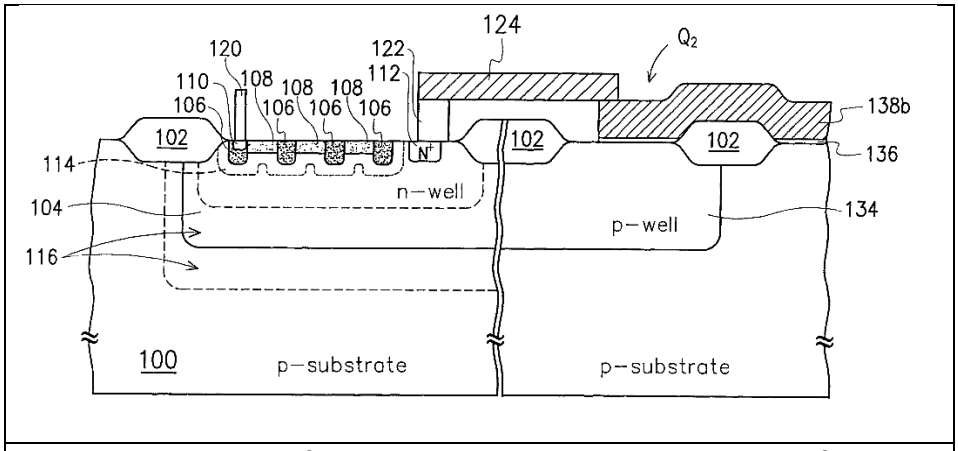

Figure 4: Schematic of the image sensor structure consisting of two regions: the image-sensing region formed in the *n*-well and the circuit region formed in the *p*-well [30].

This design consists of an image-sensing region followed by a circuit region. The image-sensing region is formed in an *n*-well in a *p*-type substrate, while the circuit region is formed in a *p*-well in a *p*-type substrate. The field oxide layer is used to isolate these two regions [30].

The image-sensing region [30] consists of two *p*-*n* photodiodes, with different depletion region thicknesses.

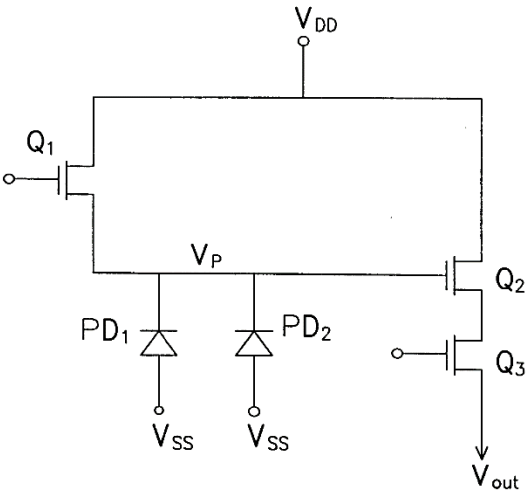

Figure 5: Equivalent circuit diagram of the image sensor structure [30].

These different depletion region thicknesses allow different wavelengths of light to be preferentially absorbed, since the most strongly absorbed wavelengths would be almost exclusively absorbed in thin depletion regions, whereas a thicker depletion region would absorb a broader spectrum, so that red, blue, and green light may be better differentiated from one another. This image sensor is also formed without increasing the layout area in comparison with the conventional structure [30]. This device is capable of measuring the entire visible spectrum, from 400 nm to 700 nm, using a CMOS based design, instead of charge-coupled devices (CCDs), which have been traditionally used for digital sensors for image capture. Therefore, this design can avoid the unwanted high fabrication costs and limitations in size reduction associated with these devices. As such, these devices are capable of being integrated in low-cost, small size, sensing systems [30].

P-i-n photodiodes are also commonly integrated with inverted rib InP or GaInAsP waveguides grown on InP substrates [31]. Such a design is fairly simple, only requiring one-step epitaxy. The structure of the waveguide is represented below:

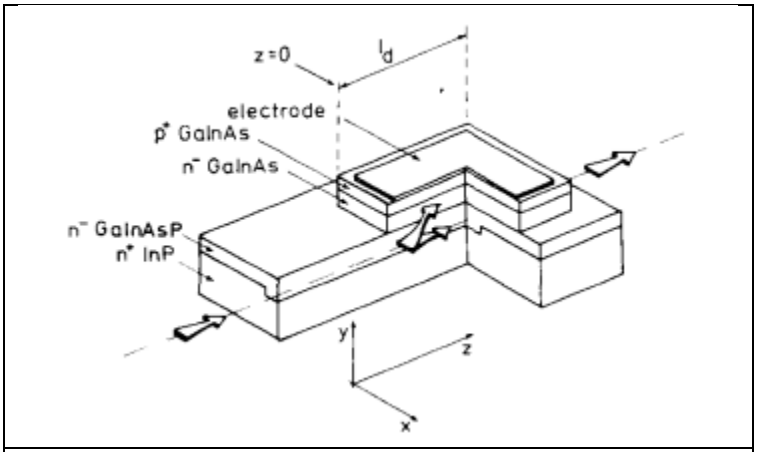

Figure 6: Schematic of the waveguide with the integrated GaInAs *p-i-n* photodiode on top [31].

This design consists of an inverted waveguide and a GaInAs *p-i-n* diode, which is formed by the GaInAs n^- layer and the n^- waveguide region (InP or GaInAsP) between the top p^+ GaInAs and the n^+ InP substrate [31]. Clearly, absorption in this photodiode is highly dependent on the waveguide structure, the wavelength, and the quaternary composition.

Although Schottky photodiodes may be used for highly sensitive ultraviolet light detection [32], photomultiplier tubes have historically been used for ultraviolet light detection due to their typically larger gain and quantum efficiency. However, there is recent demand for semiconductor-based solid-state photodetectors, due to their smaller size, lower cost, and lower power consumption. ZnO, a wide bandgap semiconductor material, has potential for application in UV light-emitting diodes and lasers, as stimulated UV emission from optically pumped thin films has been recently demonstrated [32]. Advantages of Schottky diodes for UV detection include fabrication simplicity, reasonably high quantum efficiency, and high UV/visible contrast [32]. Yet it is challenging to fabricate a Schottky diode interface with minimal interfacial traps, which can lead to high dark current, and therefore low signal-to-noise ratio. One possible alternative to a metal-ZnO junction, however, is conducting polymer, poly(3,4-

ethylenedioxythiophene) poly(styrenesulfonate) (PEDOT:PSS), which has been shown to produce a simple, high-quality Schottky contact to both Zn- and O-polar ZnO [32].

In such a design, this polymer serves as the anode when contacted to $Mg_xZn_{1-x}O$ thin films, composed of different Mg mole fractions [32]. The spectral response of such a ZnO-based Schottky photodiode has been measured using a monochromatized Xe lamp as a light source [32], and zero-bias responsivity, $R_\lambda = \frac{|I_{sc}|}{A_{opt}P_\lambda} = \rho q/hf$, was determined as a function of wavelength of the incident light (see Figure 7 below).

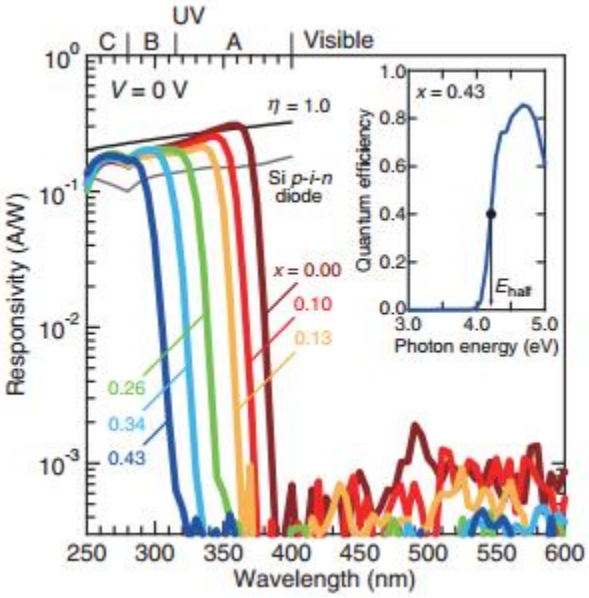

Figure 7: Spectral response of the PEDOT:PSS/$Mg_xZn_{1-x}O$ schottky diodes with zero bias at room temperature. The black and gray lines correspond to a unity quantum efficiency and the zero-bias responsivity for the Si *p-i-n* photodiode, respectively. The inset shows quantum efficiency as a function of photon energy for the x=0.43 sample with the position of E_{half} [32].

In this case, good UV/visible contrast (10^3) was observed in each of the PEDOT:PSS/$Mg_xZn_{1-x}O$ Schottky diodes with differing values of Mg content, x. The cut-off wavelength was also shown to decrease with an increase in Mg content, x, due to the widening of the bandgap energy E_g of $Mg_xZn_{1-x}O$. Thus, the cut-off energy could be varied by changing x, keeping high quantum efficiency near unity and small E_{Urb}, or the steepness in the photoresponse, up to sufficiently high Mg content ($x \leq 0.43$) [32].

While these basic photodiodes enjoy widespread use today, recent demand for high data transfer rates for telecommunications have led to the use of photodiodes in high speed long-haul and metro fiber optic communication systems. At such high optical power, these photodiodes can exhibit high levels of nonlinearity and are typically the limiting factors on quantum responsivity and bandwidth of the entire system. Thus, recent research has been focused on characterizing and minimizing this nonlinearity [1-3].

A device or system is said to be nonlinear if its output is not linearly related to its input(s). Nonlinearity is especially pronounced in avalanche photodiodes [1-3] due to the sensitivity of the impact ionization process on dynamic bias conditions. Nonlinearity may also be observed, however, in unity-gain *p*-*n* and *p*-*i*-*n* photodiodes due to a multitude of factors including 1) the velocity/field relationship of electrons and holes, 2) illumination-dependent responsivity, 3) illumination-dependent capacitance, and 4) dynamic biasing due to coupling to an external circuit [1-3]. These effects are summarized below.

Photodiodes are typically biased such that the electric field within the depletion region is large enough for photogenerated electrons and holes to travel at what is known as their saturated drift velocities [1-3]. A common misconception is that saturated drift velocities are constant; instead, they are a weak function of electric field strength. With increasing optical illumination,

photogenerated electron and hole densities can become comparable in magnitude to the background doping densities, in which case the electric field within the depletion region is redistributed even if the applied bias remains the same, as a direct consequence of the Poisson equation [1-3]. Moreover, this redistribution of the electric field in response to strong optical stimulation can also affect the thickness of depleted material, and hence the transit times of photogenerated electrons and holes to their respective depletion region boundaries where they are collected [1-3]. An indirect demonstration of this may be seen in Figure 8, where photodiode current in response to a sinusoidal stimulus is shown for two different optical illumination intensities.

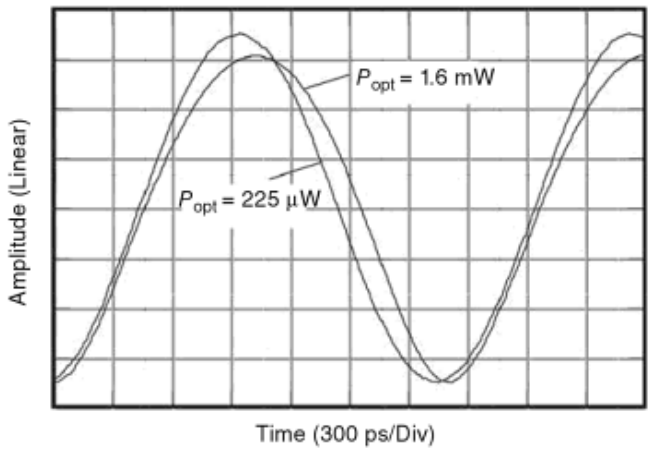

Figure 8: Oscilloscope capture of a 500-MHz photodiode signal at 225 µW and 1.6 mW demonstrating its distortion [1].

According to Esman and Williams, nonlinear responsivity may be represented as a function of photocurrent [1-3]. Consider the following plot of comparing the photocurrents of linear and nonlinear photodiodes in response to sinusoidal optical stimulus:

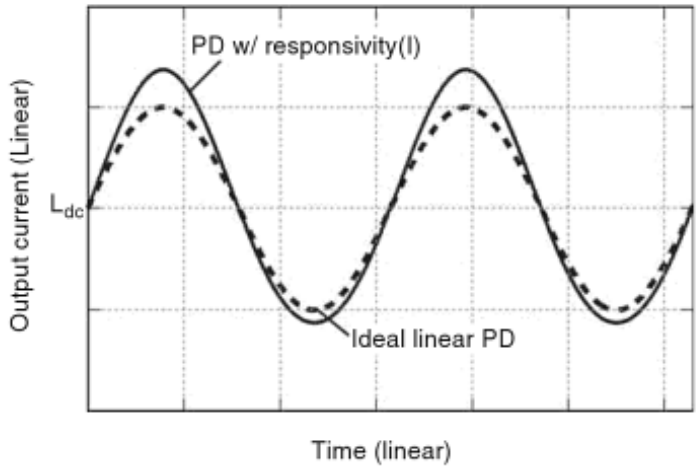

Figure 9: Output current versus time for an ideal linear photodiode versus a nonlinear photodiode with responsivity as a function of photocurrent [1].

In the figure above, the output current for the nonlinear photodiode deviates from that of the ideal photodiode, resulting in slightly larger peak output current, and a slightly lower minimum output current. On fast time scales, nonlinear responsivity can be attributed to bandgap-narrowing (a many-body quantum effect) and optical bleaching (the Burstein-Moss effect), and on longer time scales both nonradiative and radiative recombination, may contribute as well [1-3].

At sufficiently high field strengths, the Franz-Keldysh effect may also influence responsivity. The Franz-Keldysh effect [1-3] is essentially an enhancement in the rate of photon absorption through the additional energy and momentum electrons can gain from the quasi-static field during the time of interaction with a photon. Figure 10 shows the spectral responsivity of a photodiode for different levels of applied DC bias, which can be directly correlated to different values of electric field within the depletion region. The influence of the Franz-Keldysh effect is especially pronounced at the longest wavelengths, corresponding to sub-bandgap photons [1-3].

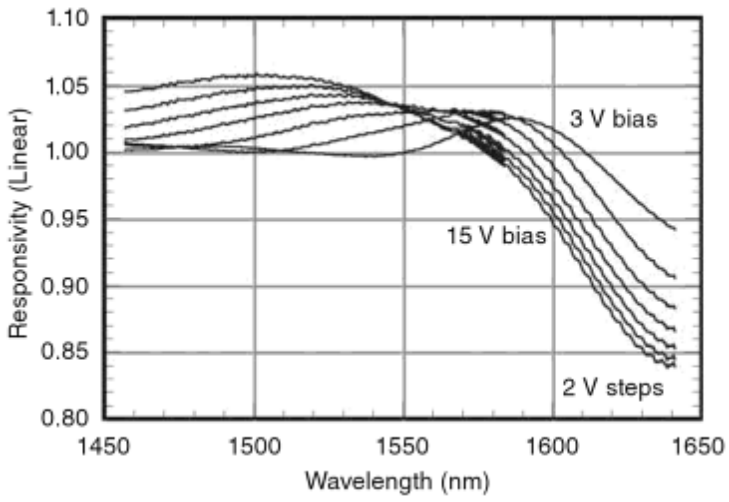

Figure 10: Measured responsivity versus wavelength for various applied voltages. All curves are normalized to the responsivity at 3 V and 1550 nm [1].

Far away from the band edge (at shorter wavelengths), the Franz-Keldysh effect becomes negligible compared to the influence of avalanche generation [1-3].

Nonlinearity can also be introduced through a photocurrent-dependent capacitance [1-3]. A simplified large-signal equivalent circuit of a photodiode is shown in Figure 11 below, where the junction capacitance appears in parallel with the source of photocurrent [1-3].

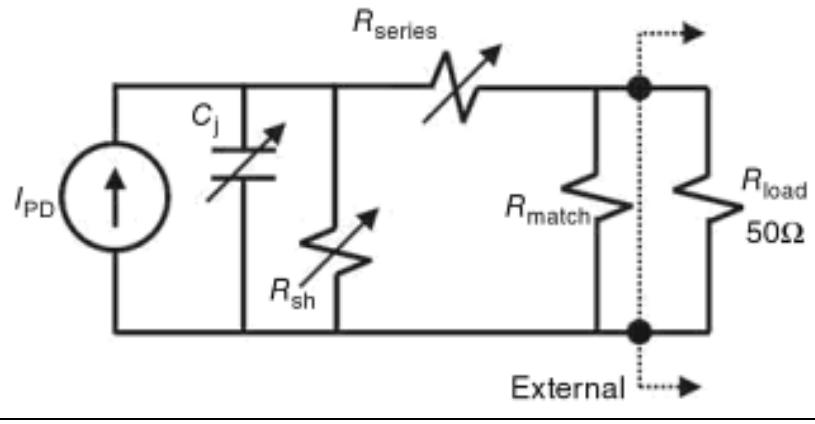

Figure 11: Photodiode equivalent circuit showing the dependence of nonlinearity on photocurrent or terminal voltage [1].

Under sufficiently high levels of optical illumination, the density of photogenerated electrons and holes within the depletion region can become comparable to that of the doping density [1-3], resulting in a redistribution of the electric field strength within the photodiode even under constant voltage conditions; this leads to a weaker average electric field, but also to a thicker depletion region, and this thicker depletion region results in a photocurrent-dependent reduction in capacitance [1-3]. This effect may be visualized by considering the small-signal single-pole R-C photocurrent response as a function of normalized frequency [1-3], as depicted in Figure 12 below.

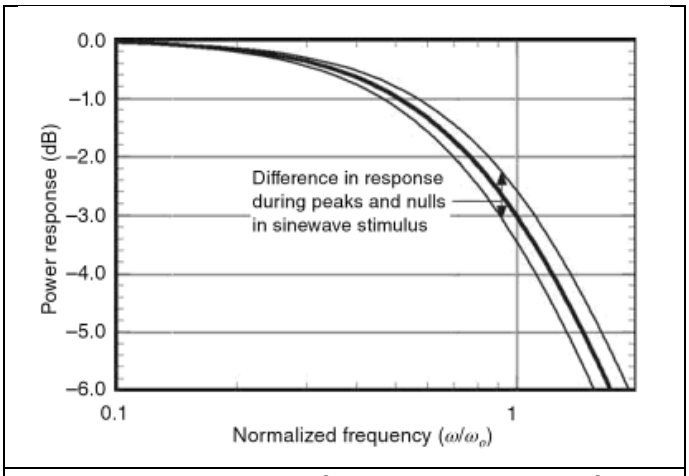

Figure 12: Normalized frequency response of a single-pole R-C filter plotted against that with a lower capacitance (top curve) and a higher capacitance (bottom curve) [1].

The response curves with slightly higher and lower capacitances represent equivalent capacitance curves at the peaks and nulls of a sinewave [1-3]. Thus, the R-C roll-off during the peaks will be different than the R-C roll off during the nulls of the sinusoid during its oscillation around its average value, resulting in an increase in photocurrent at the peak/null and a suppression of the other. These effects only occur if the device is fast enough or that the change in capacitance happens faster than the photocurrent changes [1-3].

Nonlinear capacitance can also be expressed through changes in diode voltage, even if the intensity of optical illumination remains constant, when the photodiode is integrated with an external circuit [1-3]. Specifically, any voltage transients due to photocurrent flowing through the load impedance will cause the photodiode terminal voltage to change dynamically during modulation, resulting in a nonlinear change in junction capacitance [1-3].

In addition to these common sources of nonlinearity, other effects can contribute to this as well, such as temperature fluctuations [1-3], albeit on far longer time scales than are important for high speed applications.

While all photodiodes can exhibit nonlinearity under high power conditions, two of the most commonly used photodiodes for contemporary applications are avalanche photodiodes [19, 37] and uni-traveling carrier (UTC) photodiodes (PDs) [4-7].

Pioneering work on avalanche photodiodes [19, 37] was performed by McAfee and McKay in 1963, as photodiodes gained popularity in the optoelectronics industry. A typical homojunction avalanche photodiode consists of a heavily doped n^+ region, followed by a doped p region, followed by a nearly intrinsic region (lightly doped p region), followed by a heavily doped p^+ region, as depicted in Figure 13 below.

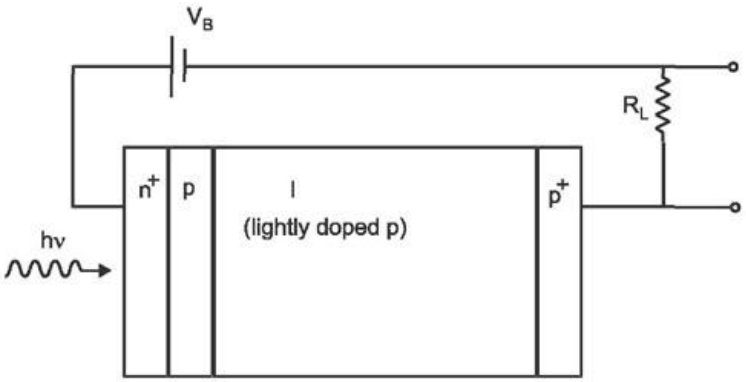

Figure 13: Band diagram of an avalanche PD under low optical illumination [37].

In contrast to *p*-*i*-*n* and other unity-gain photodiodes, avalanche photodiodes generate internal gain [19, 37]. Because the voltage signal generated from a *p*-*i*-*n* photodiode is often quite small, transimpedance amplifiers (TIAs) are commonly used, which introduce cost and complexity in a receiver system. Because of their internal gain, avalanche photodiodes can obviate the need for TIAs in many applications, though at the expense of the introduction of multiplication noise and the resultant degradation in signal-to-noise ratio [19, 37].

Impact ionization [19, 37] occurs when a free electron is accelerated in a high electric field, and gains enough kinetic energy (more than the bandgap energy), to collide with a valence electron and promote it to the conduction band, leaving behind a hole in the valence band [19, 37]. Both the original electron, as well as the new free electron and hole, may be accelerated in the electric field to high energies once again, where they each may initiate new impact ionization events [19, 37]. Such a sequence of impact ionization events leads to a geometric increase in the number of free charge carriers that may be produced by a single photon, and this process is commonly referred to as "avalanche generation" [19, 37].

As illustrated in the band diagram in Figure 13, the junction width between the leftmost n^+ and p regions is small since it is heavily and almost equally doped [19, 37]. The high electric field is confined to this region with a smaller, constant electric field in the nearly intrinsic region. Light is absorbed primarily in the large intrinsic region, where a photon with sufficient energy, greater than the bandgap energy, generates an electron-hole pair. The electrons drift toward the n^+ region while the holes drift toward the p region, due to the electric field. When the electrons enter the high field region, they initiate impact ionization, and trigger avalanche multiplication [19, 37]. Avalanche multiplication leads to a large gain, resulting in a high sensitivity. However, because a high amount of energy is needed for avalanche multiplication, a high reverse bias is needed [19, 37].

Introduced by Ishibashi *et al.* in 1997, the uni-traveling carrier (UTC) photodiode [4-7] is commonly used today for high speed and high power systems, which relies solely on the contribution of electrons to the photocurrent. A UTC PD [4-7] may be represented as a simple epitaxial layer structure consisting of a heavily-doped *n*-type contact layer, followed by an undoped *n*-type carrier collection layer, a *p*-type absorption layer, and a heavily-doped *p*-type

contact layer. An example of this is shown below for a UTC PD under reverse bias and weak optical illumination:

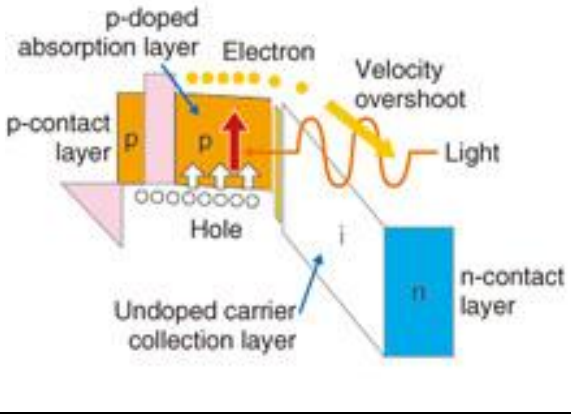

Figure 14: Band diagram of a UTC PD under low optical illumination [7].

Electrons photogenerated [4-7] in the quasi-neutral *p*-type absorption region diffuse towards the opposite direction of the drift but are blocked by the blocking layer, redirecting the electrons towards the *p*-side depletion region boundary, where they are swept across through the depletion region by the large electric field, and are ultimately collected as they hit the *n*-side depletion region boundary. Because the absorption region is quasi-neutral and *p*-type, the concentration of photogenerated majority holes is negligible compared to the background hole density, and it is the latter which determines the majority hole response. Careful solution of moments of the Boltzmann equation reveals that the primary action of the majority hole concentration in the quasi-neutral *p*-type region is to maintain quasi charge neutrality conditions, and that their contribution to the total photocurrent is usually negligible [4-7]. Thus, the charge transport in a UTC photodiode is driven by electrons as opposed to the *p*-*i*-*n* PD where both

electrons and holes contribute to the charge transport and photoresponse [4-7]. The following diagram illustrates this essential difference:

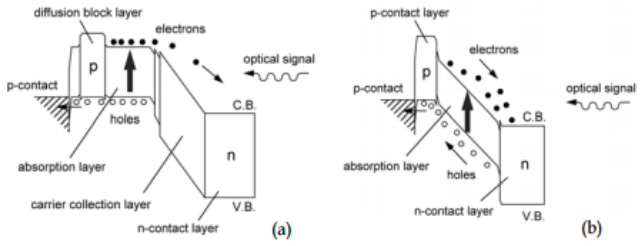

Figure 15: Band diagram and equivalent circuit model illustrating the difference in photoresponse in a) a UTC PD and b) a *p-i-n* PD under low optical illumination [6].

This characteristic leads to several key advantages for the UTC PD [4-7]. Because electrons are faster than holes, this leads to a higher operation speed. This higher operation speed also leads to another advantage of the UTC PD, which is its higher dynamic range. In any photodiode, current saturation occurs when the concentration photo-generated charges rises to high levels in the depletion layer, leading to a decrease in the electric field and an increase in depletion region thickness, affecting charge carrier transit time and degrading modulation bandwidth. Since the carrier motion of the UTC PD is dominated by electrons, which have a higher velocity than holes, the output current saturation does not occur until much later, leading to a higher dynamic range for the UTC PD [4-7].

Finally, the faster electron velocity which dominates the UTC PD photoresponse also leads to lower voltage required for operation at a given modulation frequency [4-7]. Thus, the fast electron motion in the UTC PD can be maintained by very low applied voltage, leading to smaller power consumption, less heat sinking, a lower cost, and better reliability [4-7].

Nonlinearity was later found to cause deleterious effects for most systems, including analog optical links for telecommunications [12-18, 33]. Even under moderate optical signal power, nonlinearity can lead to intermodulation distortion. Intermodulation distortion [12-18, 33] results from a nonlinear amplitude modulation of signals consisting of a superposition of two or more frequencies simultaneously. Intermodulation between each frequency component will form additional signals at frequencies at sums and differences of multiples of the original frequencies [12-18, 33].

In a linear system, the principle of superposition applies, and an input signal produces an output signal of the same frequency, yet generally of different magnitude and phase [12-18, 33]:

$$A\cos(\omega_A t + \varphi_A) \rightarrow \mathrm{B}\cos(\omega_A t + \varphi_B) \tag{1}$$

Intermodulation distortion [12-18, 33] occurs when two or more frequencies serve as inputs to a nonlinear system:

$$A_1\cos(\omega_1 t + \varphi_1) + A_2\cos(\omega_2 t + \varphi_2) \tag{2}$$

In the limit of weak nonlinearity, the spectrum of the output signal [12-18, 33] will include contributions at sums and differences of the input frequencies:

$$k_1\omega_1 + k_2\omega_2 \tag{3}$$

where k_1 and k_2 are arbitrary integers and $|k_1| + |k_2|$ is the order of the system and each signal has a distinct amplitude and phase.

Therefore, intermodulation distortion leads to a loss in output power at the fundamental frequencies, which leads to a loss in quantum efficiency and bandwidth [1-3]. Intermodulation distortion also leads to undesirable channel crosstalk in wavelength division multiplexed communications systems [1-3].

As such, it is imperative to evaluate and minimize this manifestation of nonlinearity [1-3]. One of the most common ways to assess the modulation bandwidth of a linear (or weakly

nonlinear) photodiode is through its frequency response [12-18]. A frequency response [12-18] contains key information about the behavior of the phasor components of a system. It is a measure of the amplitude and phase versus frequency.

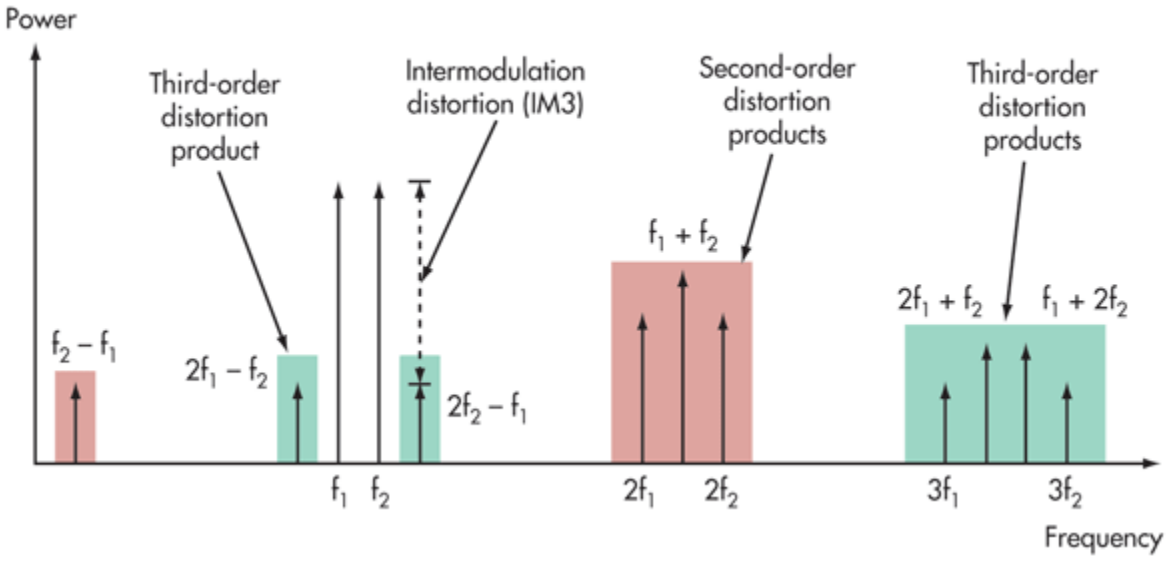

Figure 16: Example of nonlinear electrical response to two-tone optical stimulus [18]. For a purely linear system, the output power would only have frequency components at the stimulus frequencies, f_1 and f_2.

Consider next a weakly nonlinear photodiode excited by a two-tone optical stimulus at frequencies f_1 and f_2, as depicted in Figure 16. When the output signal, e.g. the voltage across a load resistance in an external circuit, is not linearly related to the input, the spectrum of the output power, which is proportional to the magnitude of this voltage squared, can be described as harmonic sums and differences of the stimulus frequencies [12-18, 33]:

$$P(\omega) = \sum_l P_l \cos(\omega_l t + \varphi_l) \quad (4)$$

where $\omega_l = k_1\omega_1 + k_2\omega_2$, and k_1 and k_2 are arbitrary integers.

The output power at the first order harmonic frequency will be exponentially greater than the

output power at the second order harmonic frequency which will also be exponentially greater than the output power at the third order harmonic frequency [12-18, 33]. As such, this frequency response can be used to obtain the behavior of the phasor components which describe intermodulation distortion [12-18, 33].

Nonlinearity can also be assessed using the IMD3 figure of merit, which represents the power in the third order interharmonic [12-18, 33]. An IMD3 plot typically shows the variation in electrical output power as a function of optical input power, at the fundamental frequencies as well as the third order interharmonic. On such a plot, the point at which the two curves intersect is called IP3, another figure of merit which helps assess the photodiode's dynamic range. In normal operation, the optical power of the input signals stimulating a photodiode remain well below IP3 [12-18, 33].

In principle, it is possible to study the nonlinear operation of photodiodes in the time domain [12-18, 33]. Time-domain analysis runs into some key issues when it is applied to large-signal distortion in semiconductor devices, however. Some voltage sources may have very narrow or very widely spaced frequencies which necessitates integration over a large number of periods of the highest frequency sinusoid. Extremely long time constants can also arise from the linear bias and filters which require an integration over many periods of the lowest-frequency sinusoid. Other issues, such as accuracy, causality, and stability problems can occur when a device is simulated in the time domain through convolution [12-18, 33].

The application of the harmonic balance method to semiconductor transistors was pioneered by B. Troyanovsky *et al.* [33]. In contrast to time domain analysis, the harmonic balance method solves nonlinear equations in the frequency domain for the large-signal steady-state response and does not exhibit problems related to time constants, tone spacings, and

incommensurate frequencies. Although the application to photodiodes in the following sections will differ, a brief review of Troyanovsky *et al.*'s harmonic balance implementation [33] follows:

Voltage sources may be treated as one- ($A_1 \neq 0$ and $A_2 = 0$) or two-tone ($A_1 \neq 0$ and $A_2 \neq 0$) sinusoids:

$$V(t) = A_1 \cos(\Omega_1 t + \varphi_1) + A_2 \cos(\Omega_2 t + \varphi_2) \quad (5)$$

where Ω_1 and Ω_2 are very closely spaced frequencies. Three-tone and higher analyses are usually not used because they can be computationally expensive and impractical.

A discretized set of drift-diffusion equations are first formulated in the time domain by incorporating three state variables at each internal device node with K internal nodes, representing electrostatic potential ψ_k, electron concentration n_k, and hole concentration p_k, along with state variables $v_l$which represents the voltage at each electrode l terminals connecting the device to its surrounding linear network in the following equation for the state vector:

$$x = [\psi_1, n_1, p_1, \dots, \psi_k, n_k, p_k, v_1, \dots, v_L] \quad (6)$$

Then, under the assumption that all state variables can be written as sums of sinusoidal basis functions:

$$x_n(t) = X_{n0}^R + \sum_{h=1}^{H} (X_{nh}^R \cos(\omega_h t) - X_{nh}^I \sin(\omega_h t)) \quad (7)$$

where $X_{nh} = X_{nh}^R + jX_{nh}^I$, where X_{nh}^R is the real and jX_{nh}^I is the imaginary part of X_{nh}, the time-domain equations are Fourier transformed, resulting in a system of simultaneous equations for the phasor state vector at each of the frequencies of the chosen basis. Then the Fourier coefficients X_{nh} can be calculated so that the equations are satisfied to within a pre-determined tolerance and describe the state variables along with the state vector X:

$$X = [X_1, X_2, \dots, X_N]^T \quad (8)$$

where $X_n = [X_{n0}^R, X_{n1}^R, X_{n1}^I, \dots, X_{nH}^R, X_{nH}^I]^T$.

In a two-tone analysis, each frequency represented in the basis of state vectors can also be described as a linear combination of the frequencies of the stimulus:

$$\omega_{k_1 k_2} = k_1\Omega_1 + k_2\Omega_2 \quad (9)$$

for k_1 and k_2 integers.

Using this model, a set of harmonic balance equations were derived by B. Troyanovsky *et al.* and used to model signal distortion in a MOSFET [33]:

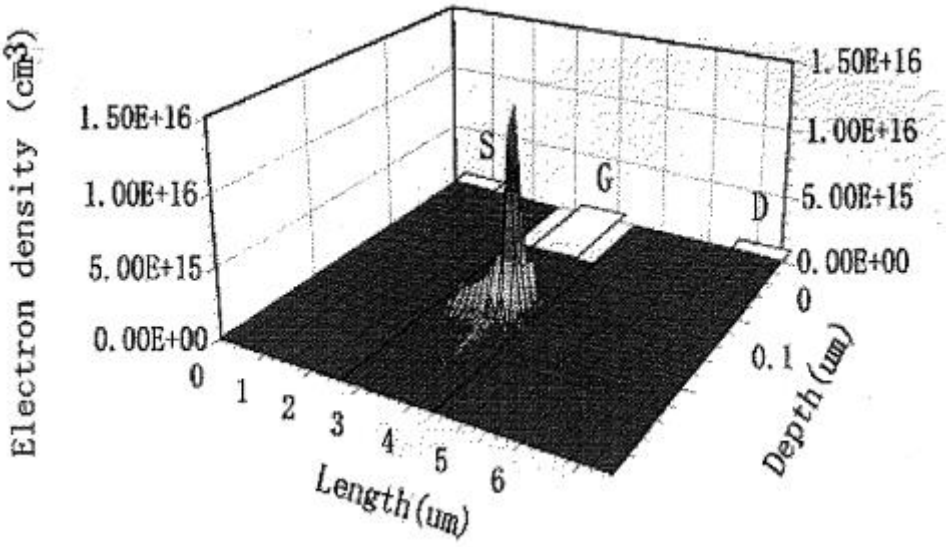

Figure 17: Distortion in electron concentration inside the MOSFET used [33].

In a recent experimental study of nonlinear responsivity in *p-i-n* photodiodes, A. Hastings *et al.* [34] minimized nonlinearities in *p-i-n* photodiodes by offsetting voltage-dependent responsivity effects caused by impact ionization and the Franz-Keldysh effect. When a large electric field is applied, the optical absorption spectrum of a PD may be altered due to the Franz-Keldysh effect. Moreover, the spatial profile of optical absorption is frequency-dependent, which in turn introduces a frequency-dependence of the responsivity contributed by avalanche generation. Because both of these effects influence the number of electron-hole pairs contributing to the photocurrent, they contribute to a so-called responsivity-based nonlinearity,

and can, at least for a certain optical wavelength, be effectively offset at a certain voltage bias to minimize this form of nonlinearity [34].

Hastings *et al.* characterized these effects as a function of incident photon energy and bias voltage [34].

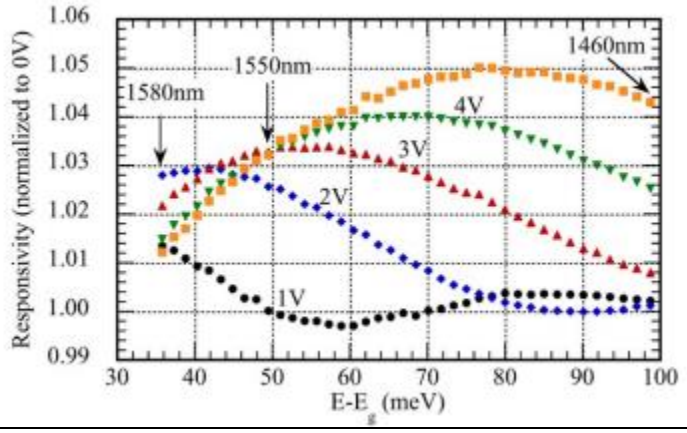

Figure 18: Measured responsivity as a function of incident photon energy, for an incident optical power of 100 µW [34].

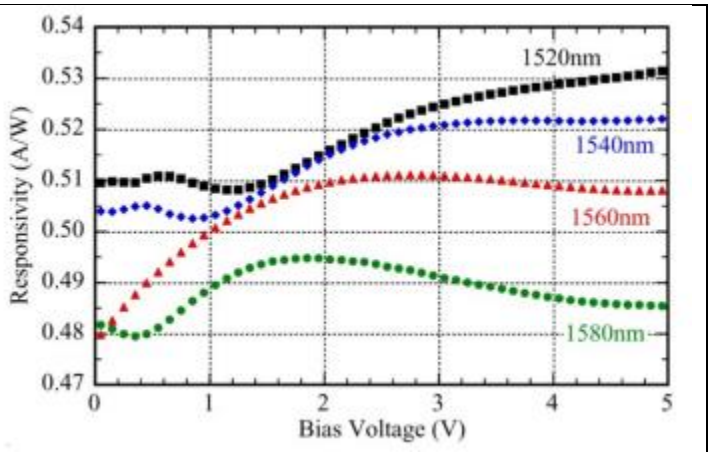

Figure 19: Measured responsivity as a function of bias voltage, for an incident optical power of 100 µW and wavelengths of 1520-1580 nm [34].

In Figure 18, the oscillatory behavior, a fingerprint of the Franz-Keldysh effect, can be seen. Impact ionization can also be detected in the peaks of these curves, which are a function of bias voltage. The peaks of this curve are fairly consistent, also indicating that the effect of impact ionization on responsivity is wavelength independent [34].

Figure 19 further describes this effect as a function of bias voltage. The FKO can be seen to dominate at <2 V bias for the 1520 nm curve. However, as voltage increases, impact ionization begins to dominate over FKO, resulting in an increase in responsivity. The FKO can also be seen to have a larger effect as the wavelength is increased, compensating for the impact ionization effect. Thus, it can be noted that at a certain bias voltage and wavelength, these two effects can offset each other, minimizing nonlinearity in *p-i-n* photodiodes [34].

H. Pan *et al.* [35] also minimized nonlinearity in an InGaAs/InP charge compensated modified uni-traveling carrier photodiode. Peaks were seen to occur in the third-order local intercept point (IP3) plot versus photocurrent, due to voltage-dependent and photocurrent-dependent capacitance effects.

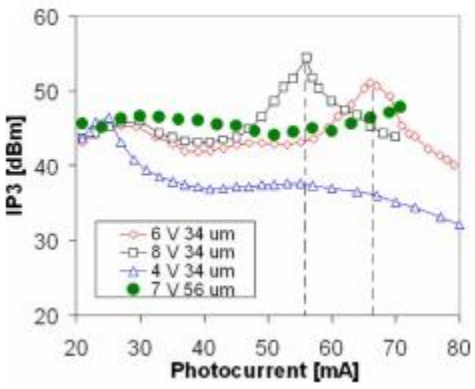

Figure 20: IP3 plot for a 34 µm and a 56 µm device as a function of photocurrent and bias voltage, exhibiting peaks for certain photocurrent and bias voltage [35].

At the position of these peaks, the two effects cancel out. As observed in their previous research, when the photocurrent increases, the capacitance of the MUTC-PD decreases. However, the voltage-effect leads to a decrease in voltage across the photodiode due to the increase in photocurrent, leading to an increase in capacitance. Thus, these two effects can be used to cancel each other out at a specific photocurrent and bias voltage. As such, the research team measured the capacitance due to photocurrent (C(I)) and the capacitance due to bias voltage (C(V)):

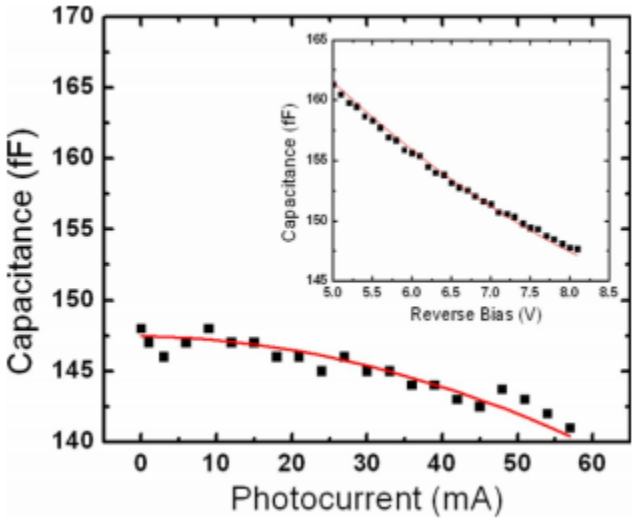

Figure 21: Measured photocurrent-dependent capacitance C(I) with quadratic fit at a reverse bias of 8 V. Measured voltage-dependent capacitance C(V) with quadratic fit at dark condition (inset) [35].

Thus, using these curves, a certain bias voltage and photocurrent were derived which would minimize these effects [35].

H. Pan *et al.* [36] characterized the nonlinearity in an InGaAs/InP charge compensated modified uni-traveling carrier photodiode using a two-tone setup. The responsivity and capacitance effects were described using an equivalent circuit model shown in Figure 22 below:

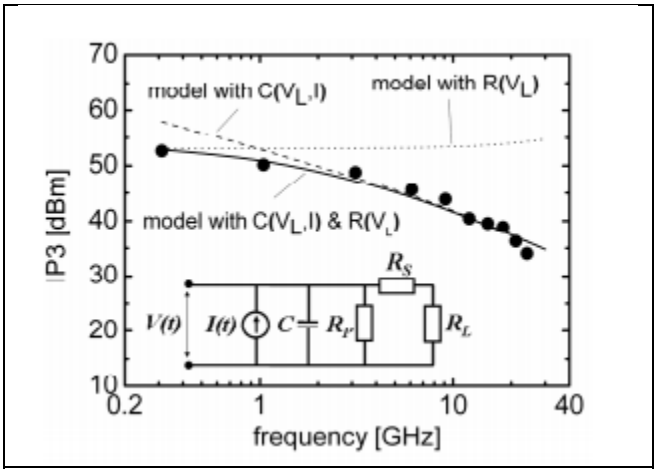

Figure 22: Measured IP3 (circles) at 50 mA and reverse bias $V_b = -7$ V, and calculated IP3 based on the voltage-dependent responsivity (dotted line), capacitive effects (dashed line) and all effects (solid line); PD equivalent circuit (inset) [36].

As can be seen in the figure above, the voltage-dependent responsivity effect dominates at low frequencies while the capacitive effects dominate at higher frequencies. However, both effects contribute to the entire, overall IP3 [36].

CHAPTER 3
DERIVING THE PHYSICS-BASED MODEL

Because of its high operation speed, bandwidth, and simplicity, a uni-traveling carrier photodiode (UTC-PD) was chosen to be the focus of this study. A physics-based model was derived which relates the electrical response of a UTC-PD to its optical stimulus. This electrical response was characterized in terms of the diode voltage (v_{diode}), the depletion region thickness (x_c), and the electric field at the beginning of the depletion region ($E(x_b)$). In this device, an InGaAs absorption region was *p*-doped to the level $5x10^{17}\ cm^{-3}$ with a thickness of 100 nm, followed by a thick InP depletion region *n*-doped at $5x10^{16}\ cm^{-3}$, above a heavily *n*-doped sub-collector region. This model is described in the diagram below:

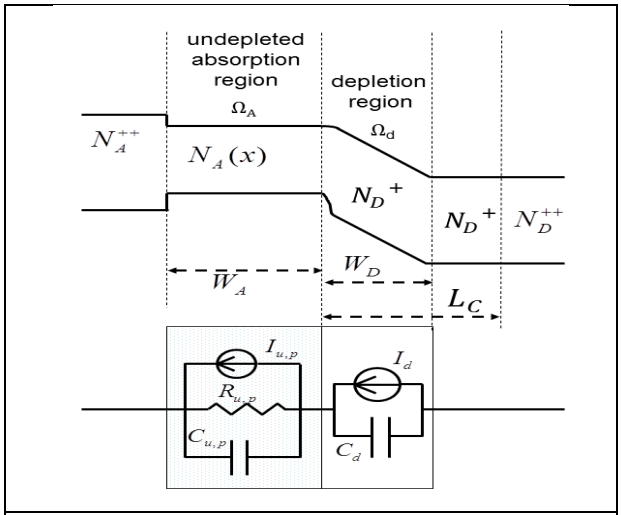

Figure 23: Band diagram and equivalent circuit model of UTC PD under low optical illumination (Courtesy of Dr. Yoder).

In anticipation of applying the harmonic balance method [33] to study this UTC PD device structure, each solution variable will be represented as linear combinations of phasor quantities,

at a set of frequencies which are in turn linear combinations of the stimulus frequencies. Assuming a two-tone analysis (ω_a and ω_b), the optical stimulus may be represented as a volumetric electron-hole pair generation rate $G(t)$ as follows:

$$G(t) = G_a^+ e^{j\omega_a t} + G_a^- e^{-j\omega_a t} + G_b^+ e^{j\omega_b t} + G_b^- e^{-j\omega_b t} \quad (10)$$

Unknown quantities characterizing the response of the photodiode may then be represented as

$$x_c = \sum_l x_c^l e^{j\omega_l t} \quad (11)$$

$$J(x) = \sum_l J^l(x) e^{j\omega_l t} \quad (12)$$

$$v_{diode} = \sum_l v_{diode}^l e^{j\omega_l t} \quad (13)$$

$$n(x) = \sum_l n^l(x) e^{j\omega_l t} \quad (14)$$

where x_c is the depletion region thickness, v_{diode} is the diode voltage, $J(x)$ is the current density, $n(x)$ is the electron density, and $\omega_l = k_1\omega_a + k_2\omega_b$ is a linear combination of stimulus frequencies, with k_1 and k_2 constrained to a finite set of integers. In this thesis, a two tone stimulus, ω_a and ω_b, was used and only up to third order harmonics were considered for simplicity:

Table 1. Harmonic Frequencies Resulting from Two Tone Stimulus, ω_a and ω_b, Up to Third Order.

Order	Frequency
0	0
1	ω_a
	ω_b
2	$\omega_a + \omega_b$
	$\omega_a - \omega_b$
	$-\omega_a + \omega_b$

Table 1 (continued).

	$-\omega_a - \omega_b$
	$2\omega_a$
	$-2\omega_a$
	$2\omega_b$
	$-2\omega_b$
3	$2\omega_a + \omega_b$
	$2\omega_a - \omega_b$
	$-2\omega_a + \omega_b$
	$-2\omega_a - \omega_b$
	$\omega_a + 2\omega_b$
	$-\omega_a + 2\omega_b$
	$\omega_a - 2\omega_b$
	$-\omega_a - 2\omega_b$
	$3\omega_a$
	$-3\omega_a$
	$3\omega_b$
	$-3\omega_b$

Once the system of simultaneous nonlinear equations is formulated, the Newton-Raphson Method [8-11] may be used to calculate the phasor solution variables: the diode voltage (v_{diode}), the depletion region thickness (x_c), and the electric field at the beginning of the depletion region

($E(x_b)$). The Newton-Raphson Method, developed by Isaac Newton and Joseph Raphson, is a method of deriving a solution x to an equation $f(x) = 0$ through iterations based on an initial guess. In the discussion which follows, x will be a column vector of phasor solution variables, and the index j will be used to reference iteration number. The equation

$$f(x) = 0 \tag{15}$$

is linearized at the point of an initial guess for x as follows

$$f(x_j) + \frac{\partial f_j}{\partial x_j}\partial x_j = 0 \tag{16}$$

and a first order correction to this initial guess may then be calculated as follows

$$\partial x_j = -\left(\frac{\partial f_j}{\partial x_j}\right)^{-1}(f(x_j)) \tag{17}$$

A new guess is made for the next iteration according to

$$x_{j+1} = x_j + \partial x_j \tag{18}$$

and the iterative process repeats. The term $\frac{\partial f}{\partial x_j}$ can be constructed as a Jacobian matrix [38] so that each component can be represented as $J_{i,j} = \frac{\partial f_i}{\partial x_j}$:

$$J = \frac{\partial f}{\partial x} = \left[\frac{\partial f}{\partial x_1} \ldots \frac{\partial f}{\partial x_n}\right] = \begin{bmatrix} \frac{\partial f_1}{\partial x_1} & \cdots & \frac{\partial f_1}{\partial x_n} \\ \vdots & \ddots & \vdots \\ \frac{\partial f_m}{\partial x_1} & \cdots & \frac{\partial f_m}{\partial x_n} \end{bmatrix} \tag{19}$$

In this thesis, the physics-based model used to describe photodiode operation is based on the solution of four fundamental equations: a) the current continuity equation for electrons [39], b) a node voltage equation describing the interaction between the nonlinear photodiode and its external circuit [40], c) Maxwell's first equation [41], and d) the Poisson equation [42]. Within the depletion region, an analytic solution to the electron continuity equation for electron density $n(x)$ exists, and solutions to the remaining three equations will be represented in terms of the following physical quantities: the diode voltage (v_{diode}), the depletion region thickness (x_c), and the electric field at the beginning of the depletion region ($E(x_b)$).

3.1 Deriving the Three Equations Relating Diode Voltage, the Depletion Region Thickness, and the Electric Field at the Beginning of the Depletion Region

3.1.1 Equation One

The depletion region can be represented as the following figure, where J is electron current density, $n(x)$ is the electron density, x_b is the beginning of the depletion region, and x_c is the depletion region thickness:

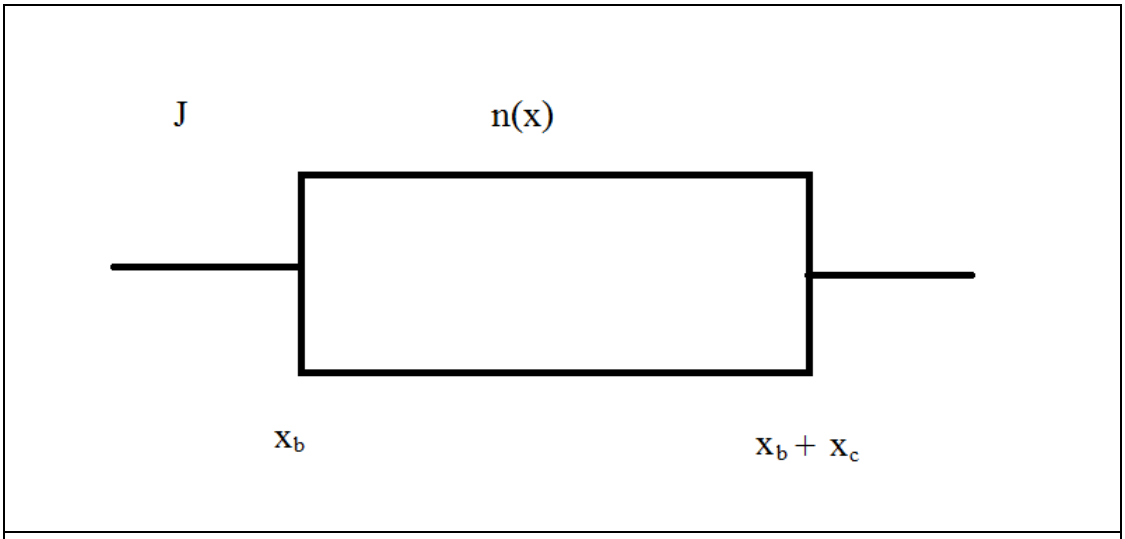

Figure 24: Band diagram representing the depletion region of the UTC PD under low optical illumination.

Within the depletion region, the continuity equation [39] for electrons reads

$$\frac{dJ_n}{dx} = q\frac{\partial n}{\partial t} \tag{20}$$

Under the assumption that electrons within the depletion region move at their saturated drift velocity, the electron current density may be written as $J_n = -qv_{sat}n$ due to the Ramo-Shockley theorem [43], with electron density $n = \sum_l n_l e^{j\omega_l t}$., substituting, one obtains

$$\frac{d}{dx}(-qv_{sat}n) = {}_jq\omega n \tag{21}$$

such that

$$\frac{d}{dx}n = -\frac{\omega}{jv_{sat}}n \tag{22}$$

and hence

$$n = n_0 e^{-\frac{\omega}{jv_{sat}}x} \tag{23}$$

Within the depletion region, therefore, LaPlace's equation [42], $\nabla \cdot E = \frac{\rho}{\varepsilon}$, reads

$$\nabla \cdot \varepsilon E = q(N_D - n(x_b)e^{-\frac{\omega}{jv_{sat}}(x-x_b)}) \tag{24}$$

$$\frac{dE}{dx} = \frac{q}{\varepsilon}(N_D - n(x_b)e^{-\frac{\omega}{jv_{sat}}(x-x_b)}) \tag{25}$$

$$E(x) = E(x_b) + \int_{x_b}^{x} \frac{q}{\varepsilon}(N_D - n(x_b)e^{-\frac{\omega}{jv_{sat}}(x'-x_b)})\,dx' \tag{26}$$

$$E(x) = E(x_b) + \frac{q}{\varepsilon}N_D(x - x_b) - \frac{qv_{sat}n(x_b)}{j\varepsilon\omega}(e^{-\frac{\omega}{jv_{sat}}(x-x_b)} - 1) \tag{27}$$

Using Maxwell's first law [41], that $v = \int E\,dx$,

$$-(v_{diode} + v_{bi}) = \int_{x_b}^{x_b+x_c} E(x_b) + \frac{qN_D}{\varepsilon}(x - x_b) - \frac{qv_{sat}n(x_b)}{j\varepsilon\omega}\left(e^{-\frac{\omega}{jv_{sat}}(x-x_b)} - 1\right)dx \tag{28}$$

$$-v_{diode} - v_{bi} = -E(x_b)x_c - \frac{qN_D}{2\varepsilon}x_c^2 + \frac{qv_{sat}n(x_b)}{j\varepsilon\omega}\int_{x_b}^{x_b+x_c}\left(e^{-\frac{\omega}{jv_{sat}}(x-x_b)} - 1\right)dx \tag{29}$$

$$-v_{diode} - v_{bi} = -E(x_b)x_c - \frac{qN_D}{2\varepsilon}x_c^2 + \frac{qv_{sat}n(x_b)}{j\varepsilon\omega}\left(\frac{v_{sat}}{j\omega}\left(e^{-\frac{\omega}{jv_{sat}}(x_c)} - 1\right) - x_c\right) \tag{30}$$

which is merely a statement of the Poisson equation, using the boundary conditions that 1) the electrostatic potential difference across the depletion region is equal to the applied diode voltage plus the built-in junction potential, and 2) the electric field at the *p*-side edge of the depletion region is $E(x_b)$.

3.1.2 Equation Two

The external circuit can be represented by the following band diagram, where L_b, C_b, and R_l represent the external RLC circuit powered by the applied voltage v_{ap}, and I_d and C_j represent the diode circuit, with the diode current I_d and the junction capacitance C_j.

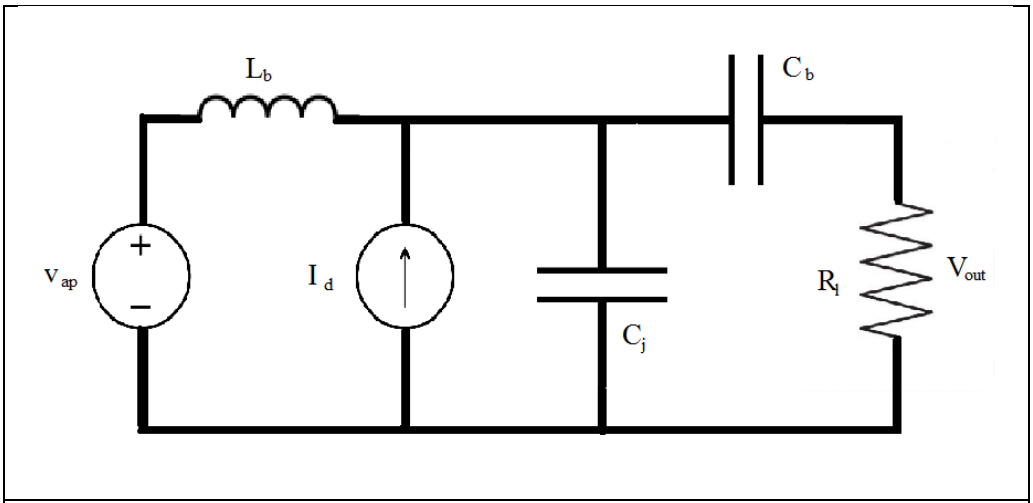

Figure 25: The UTC PD is connected to an external circuit in a bias tee configuration.

Assuming that L_b and C_b are large,

For $\omega = 0$,

$$v_d(\omega = 0) = v_{ap} \tag{31}$$

Otherwise, using Kirchoff's Circuit Law [40], that the sum of currents into a node in a closed circuit is zero,

$$I_d = \frac{v_d}{R_L} + \frac{dQ_j}{dt} \tag{32}$$

Representing the electron current density as $J = -qn(x)v_{sat}$ with $n = n_0 e^{-\frac{\omega}{jv_{sat}}(x)}$, the Ramo-Shockley theorem [43] may be invoked to evaluate the photocurrent

$$I_d = -qv_{sat}A\int_{x_b}^{x_b + x_c} n(x_b)e^{-\frac{\omega}{jv_{sat}}(x-x_b)}dx \tag{33}$$

with solution

$$I_d = -\frac{qv_{sat}^2An(x_b)}{j\omega}\frac{1}{x_c}(e^{-\frac{\omega}{jv_{sat}}(x_c)} - 1) \tag{34}$$

The stored charge within the depletion region, Q_j, may be calculated through

$$Q_j = qA\int_{x_b}^{x_b + x_c}(N_D - n(x_b)e^{-\frac{\omega}{jv_{sat}}(x-x_b)})dx \tag{35}$$

$$Q_j = qA(N_D - \frac{v_{sat}}{j\omega} n(x_b)\left(e^{-\frac{\omega}{jv_{sat}}(x_c)} - 1\right)) \tag{36}$$

After substitution, an equation relating the diode voltage (v_{diode}) to the depletion region thickness (x_c) may be written:

$$-\frac{qv_{sat}^2 An(x_b)}{j\omega}\frac{1}{x_c}\left(e^{-\frac{\omega}{jv_{sat}}(x_c)} - 1\right) = \frac{v_d}{R_l} + qA\frac{d}{dt}(N_D - \frac{v_{sat}}{j\omega} n(x_b)\left(e^{-\frac{\omega}{jv_{sat}}(x_c)} - 1\right)) \tag{37}$$

3.1.3 Equation Three

Finally, the last equation relating the depletion region thickness (x_c) to the electric field at the beginning of the depletion region ($E(x_b)$) is obtained through the integral form of Maxwell's first equation [41], i.e. Gauss's Law:

$$E(x) = \frac{q}{\varepsilon} N_D(x - x_b) - \frac{q}{\varepsilon}\int_{x_b}^{x} n(x')dx' + E(x_b^+) \tag{38}$$

Because the electric field in the quasi-neutral *n*-type material to the right of the depletion region is essentially zero, the boundary condition $E(x_c + x_b) = 0$ must be applied:

$$\frac{qN_D}{\varepsilon} x_c + E(x_b^+) - \frac{q}{\varepsilon}\int_{x_b}^{x_b+x_c} n(x')\,dx' = 0 \tag{39}$$

$$E(x_b^+) = \frac{q}{\varepsilon}\int_{x_b}^{x_b+x_c} n(x')dx' - \frac{qN_D}{\varepsilon} x_c \tag{40}$$

$$E(x_b^+) = \frac{q}{\varepsilon}\int_{x_b}^{x_b+x_c} n(x_b)e^{-\frac{\omega}{jv_{sat}}(x'-x_b)}dx' - \frac{qN_D}{\varepsilon} x_c \tag{41}$$

and finally:

$$E(x_b^+) = \frac{qv_{sat}n(x_b)}{j\omega\varepsilon}(e^{-\frac{\omega}{jv_{sat}}(x_c)} - 1) - \frac{qN_D}{\varepsilon} x_c \tag{42}$$

Equations (30), (37) and (42) represent the three simultaneous nonlinear equations which must be solved in terms of the three unknowns: diode voltage (v_{diode}), depletion region thickness (x_c), and the electric field at the beginning of the depletion region ($E(x_b)$). To facilitate analysis, a Taylor Series expansion [44-47] has been used on the complex exponentials in these equations involving the depletion region thickness, x_c. The modulation bandwidth of most UTC-PDs is RC limited rather than transit time limited, so the argument of these complex exponents, $-\frac{\omega}{jv_{sat}}(x_c)$, is expected to be small; stated differently, the average electron transit

time through the depletion region, $\frac{x_c}{v_{sat}}$, is expected to be significantly smaller than the period of the optical stimulus. To third order, a Taylor series may be expressed as follows:

$$f(x) = f(x) + \frac{f'(x)}{1!} + \frac{f''(x)}{2!} + \frac{f'''(x)}{3!} \tag{43}$$

$$f(x) = \sum_{n=0}^{\infty} \frac{f^{(n)}(x)}{n!}(x)^n \tag{44}$$

Therefore, the relevant complex exponentials in the PD model may be expanded as follows

$$e^{-\frac{\omega}{jv_{sat}}(x_c)} = 1 - \frac{\omega}{jv_{sat}}x_c - \frac{\omega^2}{2v_{sat}^2}x_c^2 + \frac{\omega^3}{j6v_{sat}^3}x_c^3 + \frac{\omega^4}{24v_{sat}^4}x_c^4 + \cdots \tag{45}$$

In this thesis, terms up to 4th order in the argument of the complex exponential are retained, representing a balance between accuracy and ease of implementation.

With these substitutions, equations (30), (37) and (42) may be rewritten as follows:

3.2 Simplifying the Three Equations Relating Diode Voltage, the Depletion Region Thickness, and the Electric Field at the Beginning of the Depletion Region

3.2.1 Equation 1

The first equation relating diode voltage (v_{diode}), the depletion region thickness (x_c), and the electric field at the beginning of the depletion region ($E(x_b)$) was derived as the following:

$$-v_{diode} - v_{bi} = -E(x_b)x_c - \frac{qN_D}{2\varepsilon}x_c^2 + \frac{qv_{sat}n(x_b)}{j\varepsilon\omega}\left(\frac{v_{sat}}{j\omega}\left(e^{-\frac{\omega}{jv_{sat}}(x_c)} - 1\right) - x_c\right) \tag{46}$$

Substituting the Taylor series for the exponential term $e^{-\frac{\omega}{jv_{sat}}(x_c)}$ into this equation,

$$-v_{diode} - v_{bi} = -E(x_b)x_c - \frac{qN_D}{2\varepsilon}x_c^2 + \frac{qv_{sat}n(x_b)}{j\varepsilon\omega}\left(\frac{v_{sat}}{j\omega}\left(1 - \frac{\omega}{jv_{sat}}x_c - \frac{\omega^2}{2v_{sat}^2}x_c^2 + \frac{\omega^3}{j6v_{sat}^3}x_c^3 + \frac{\omega^4}{24v_{sat}^4}x_c^4 - 1\right) - x_c\right) \tag{47}$$

$$-v_{diode} - v_{bi} = -E(x_b)x_c - \frac{qN_D}{2\varepsilon}x_c^2 + \frac{qv_{sat}n(x_b)}{j\varepsilon\omega}\left(\frac{v_{sat}}{j\omega}\left(-\frac{\omega}{jv_{sat}}x_c - \frac{\omega^2}{2v_{sat}^2}x_c^2 + \frac{\omega^3}{j6v_{sat}^3}x_c^3 + \frac{\omega^4}{24v_{sat}^4}x_c^4\right) - x_c\right) \tag{48}$$

$$-v_{diode} - v_{bi} = -E(x_b)x_c - \frac{qN_D}{2\varepsilon}x_c^2 + \frac{qv_{sat}n(x_b)}{j\varepsilon\omega}\left(x_c - \frac{\omega}{j2v_{sat}}x_c^2 - \frac{\omega^2}{6v_{sat}^2}x_c^3 + j\frac{\omega^3}{24v_{sat}^3}x_c^4 - x_c\right) \tag{49}$$

$$-v_{diode} - v_{bi} = -E(x_b)x_c - \frac{qN_D}{2\varepsilon}x_c^2 + \frac{qv_{sat}n(x_b)}{j\varepsilon\omega}\left(-\frac{\omega}{j2v_{sat}}x_c^2 - \frac{\omega^2}{6v_{sat}^2}x_c^3 + j\frac{\omega^3}{24v_{sat}^3}x_c^4\right) \tag{50}$$

$$-v_{diode} - v_{bi} = -E(x_b)x_c - \frac{qN_D}{2\varepsilon}x_c^2 + \frac{qn(x_b)}{2\varepsilon}x_c^2 - \frac{q\omega n(x_b)}{j6\varepsilon v_{sat}}x_c^3 - \frac{q\omega^2 n(x_b)}{24\varepsilon v_{sat}^2}x_c^4 \tag{51}$$

$$-v_{diode} - v_{bi} + E(x_b)x_c + \frac{qN_D}{2\varepsilon}x_c^2 - \frac{qn(x_b)}{2\varepsilon}x_c^2 + \frac{q\omega n(x_b)}{j\,6\varepsilon v_{sat}}x_c^3 + \frac{q\omega^2 n(x_b)}{24\varepsilon v_{sat}^2}x_c^4 = 0 \quad (52)$$

3.2.2 Equation 2

The second equation relating diode voltage (v_{diode}) to depletion region thickness (x_c) was derived as:

$$-\frac{qv_{sat}^2 An(x_b)}{j\omega}\frac{1}{x_c}\left(e^{-\frac{\omega}{jv_{sat}}(x_c)} - 1\right) = \frac{v_d}{R_l} + qA\frac{d}{dt}\left(N_D - \frac{v_{sat}}{j\omega}n(x_b)\left(e^{-\frac{\omega}{jv_{sat}}(x_c)} - 1\right)\right) \quad (53)$$

Then using the third equation, this equation can be related to the electric field at the beginning of the depletion region ($E(x_b)$):

$$-\frac{qv_{sat}^2 An(x_b)}{j\omega}\frac{1}{x_c}\left(e^{-\frac{\omega}{jv_{sat}}(x_c)} - 1\right) = \frac{v_d}{R_l} + qA\frac{d}{dt}\left(N_D - \frac{v_{sat}}{j\omega}n(x_b)\left(e^{-\frac{\omega}{jv_{sat}}(x_c)} - 1\right)\right) \quad (54)$$

$$-\frac{qv_{sat}^2 An(x_b)}{j\omega}\frac{1}{x_c}\left(e^{-\frac{\omega}{jv_{sat}}(x_c)} - 1\right) = \frac{v_d}{R_l} - A\varepsilon\frac{d}{dt}(E(x_b)) \quad (55)$$

Since the electric field at the beginning of the depletion region ($E(x_b)$) is a function of the stimulus frequency, $E(x_b) = E(x_b)e^{j\omega t}$,

$$-\frac{qv_{sat}^2 An(x_b)}{j\omega}\frac{1}{x_c}\left(e^{-\frac{\omega}{jv_{sat}}(x_c)} - 1\right) = \frac{v_d}{R_l} - A\varepsilon(j\omega(E(x_b))) \quad (56)$$

Finally, substituting the Taylor series expansion for the exponential term $e^{-\frac{\omega}{jv_{sat}}(x_c)}$ into this equation,

$$-\frac{qv_{sat}^2 An(x_b)}{j\omega}\frac{1}{x_c}\left(1 - \frac{\omega}{jv_{sat}}x_c - \frac{\omega^2}{2v_{sat}^2}x_c^2 + \frac{\omega^3}{j6v_{sat}^3}x_c^3 + \frac{\omega^4}{24v_{sat}^4}x_c^4 - \frac{\omega^5}{j120v_{sat}^5}x_c^5 - 1\right) = \frac{v_d}{R_l} - j\omega\varepsilon A(E(x_b)) \quad (57)$$

$$-\frac{qv_{sat}^2 An(x_b)}{j\omega}\frac{1}{x_c}\left(-\frac{\omega}{jv_{sat}}x_c - \frac{\omega^2}{2v_{sat}^2}x_c^2 + \frac{\omega^3}{j6v_{sat}^3}x_c^3 + \frac{\omega^4}{24v_{sat}^4}x_c^4 - \frac{\omega^5}{j120v_{sat}^5}x_c^5\right) = \frac{v_d}{R_l} - j\omega\varepsilon A(E(x_b)) \quad (58)$$

$$-qv_{sat}An(x_b) + \frac{qAn(x_b)\omega}{j2}x_c + \frac{qAn(x_b)\omega^2}{6v_{sat}}x_c^2 - \frac{qAn(x_b)\omega^3}{j24v_{sat}^2}x_c^3 - \frac{qAn(x_b)\omega^4}{120v_{sat}^3}x_c^4 = \frac{v_d}{R_l} - j\omega\varepsilon A(E(x_b)) \quad (59)$$

$$qv_{sat}An(x_b) - \frac{qAn(x_b)\omega}{j2}x_c - \frac{qAn(x_b)\omega^2}{6v_{sat}}x_c^2 + \frac{qAn(x_b)\omega^3}{j24v_{sat}^2}x_c^3 + \frac{qAn(x_b)\omega^4}{120v_{sat}^3}x_c^4 + \frac{v_d}{R_l} - j\omega\varepsilon A(E(x_b)) = 0 \quad (60)$$

3.2.3 Equation 3

The third equation relating the depletion region thickness (x_c) to the electric field at the beginning of the depletion region ($E(x_b)$) was derived as:

$$E(x_b^+) = \frac{qv_{sat}n(x_b)}{j\varepsilon\omega}(e^{-\frac{\omega}{jv_{sat}}(x_c)} - 1) - \frac{qN_D}{\varepsilon}x_c \quad (61)$$

Substituting the Taylor series expansion for the exponential term $e^{-\frac{\omega}{jv_{sat}}(x_c)}$,

$$E(x_b^+) = \frac{qv_{sat}n(x_b)}{j\varepsilon\omega}(1 - \frac{\omega}{jv_{sat}}x_c - \frac{\omega^2}{2v_{sat}^2}x_c^2 + \frac{\omega^3}{j6v_{sat}^3}x_c^3 + \frac{\omega^4}{24v_{sat}^4}x_c^4 - 1) - \frac{qN_D}{\varepsilon}x_c \quad (62)$$

$$E(x_b^+) = \frac{qv_{sat}n(x_b)}{j\varepsilon\omega}(- \frac{\omega}{jv_{sat}}x_c - \frac{\omega^2}{2v_{sat}^2}x_c^2 + \frac{\omega^3}{j6v_{sat}^3}x_c^3 + \frac{\omega^4}{24v_{sat}^4}x_c^4) - \frac{qN_D}{\varepsilon}x_c \quad (63)$$

$$E(x_b^+) = \frac{qn(x_b)}{\varepsilon}x_c - \frac{qn(x_b)\omega}{j2v_{sat}\varepsilon}x_c^2 - \frac{qn(x_b)\omega^2}{6v_{sat}^2\varepsilon}x_c^3 + \frac{qn(x_b)\omega^3}{j24v_{sat}^3\varepsilon}x_c^4 - \frac{qN_D}{\varepsilon}x_c \quad (64)$$

$$E(x_b^+) - \frac{qn(x_b)}{\varepsilon}x_c + \frac{qn(x_b)\omega}{j2v_{sat}\varepsilon}x_c^2 + \frac{qn(x_b)\omega^2}{6v_{sat}^2\varepsilon}x_c^3 - \frac{qn(x_b)\omega^3}{j24v_{sat}^3\varepsilon}x_c^4 + \frac{qN_D}{\varepsilon}x_c = 0 \quad (65)$$

Finally, a C++ program was designed in order to apply the Newton-Raphson Method to these equations to approximate the diode voltage (v_{diode}), depletion region thickness (x_c), and the electric field at the beginning of the depletion region ($E(x_b)$).

CHAPTER 4
FREQUENCY RESPONSE AND TWO-TONE MEASUREMENT

The influence of nonlinearity on the operation of a UTC PD is assessed in two ways. First, the frequency response is calculated as a function of average optical power. At high optical powers, modulation bandwidth is known to collapse as the photogenerated charge carrier density approaches that of the background doping density and begins to screen the depletion field. Second, the third-order harmonic response to a two-tone optical stimulus is calculated as a function of average optical input power. IMD3 and the associated quantity IP3 may be used to assess the severity of interharmonic distortion. In a frequency plot, output power at the single-tone fundamental frequency (ω_a) is plotted versus frequency at various levels of average photocurrent, while a two-tone stimulus is used for an IMD3 plot, and the output power at one of the first order fundamental frequencies (ω_a), as well as the output power at the third order frequency ($2\omega_a - \omega_b$) are plotted against the average optical input power.

The optical input power [19-29] may be related to the number of photons which are absorbed in the photodiode. When a photon with sufficient energy is absorbed within the photodiode, an electron-hole pair is created. This energy of a photon may be related to its frequency through the following equation:

$$E_{ph} = hf \tag{66}$$

where E_{ph} is the energy of the photon, h is Planck's constant, and f is the frequency of the light. The optical input power absorbed within the UTC photodiode, P_{in}, may then be related to the free electron density at the edge of the depletion region as follows:

$$P_{in} = Ahfv_{sat}n(x_b) \tag{67}$$

under the assumption that the time scale for electron transport through the depleted absorber is

much faster than that of electron transport through the depletion region. This is true for most UTC PD designs which have been reported in the archival literature.

The electrical output power was calculated as the power dissipated by the load resistor:

$$P_{out} = \frac{1}{2R}|v_{diode}|^2 \tag{68}$$

where P_{out} is the output power, v_{diode} is the diode voltage, and R is the load resistance (57Ω).

Figure 26 below shows the frequency response calculated for the UTC PD considered in this thesis, up to a maximum frequency of 50 GHz. Several curves are depicted, corresponding to average (DC) photocurrent levels of 10mA, 20mA, 30mA and 40mA, and considering between 1 and 4 terms in the Taylor series expansion of the complex exponential of Eqn. (45), which appears in each equation of the physics-based model used. From these curves it is evident that the Taylor series can be safely truncated after a small number of terms and that modulation bandwidth is predominantly RC-limited, consistent with the stated assumptions.

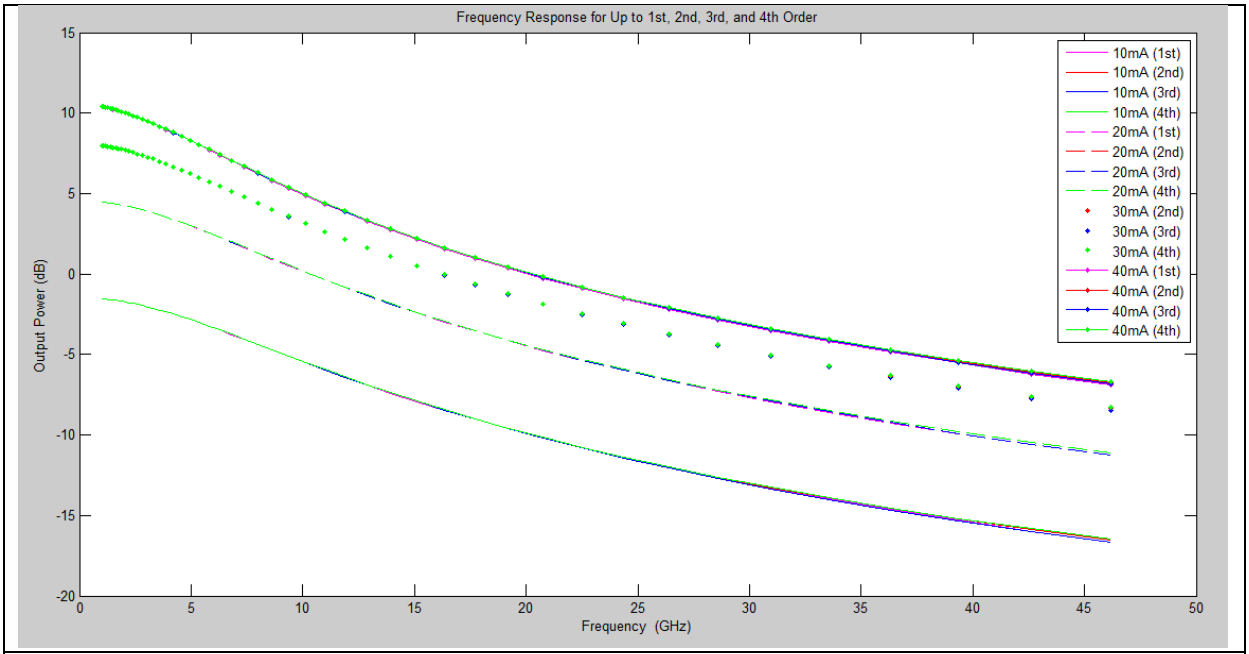

Figure 26: Frequency response for up to first order (magenta), second order (red), third order (blue) and fourth order (green) polynomial terms as a function of average photocurrent (10mA (-), 20mA (--), 30mA (.), and 40mA (.-)).

As the average optical input power is increased such that the average photocurrent exceeds 40mA, the UDC PD bandwidth collapses as the width of the depletion width increases dramatically.

The variation of low-frequency (100 MHz) IMD3 with optical input power is shown in Figure 27 below, for the cases of 1, 2, 3 and 4 terms considered from the Eqn. (45). Again, the results are indistinguishable among the various orders of truncation of the Taylor series, confirming assumptions of the model.

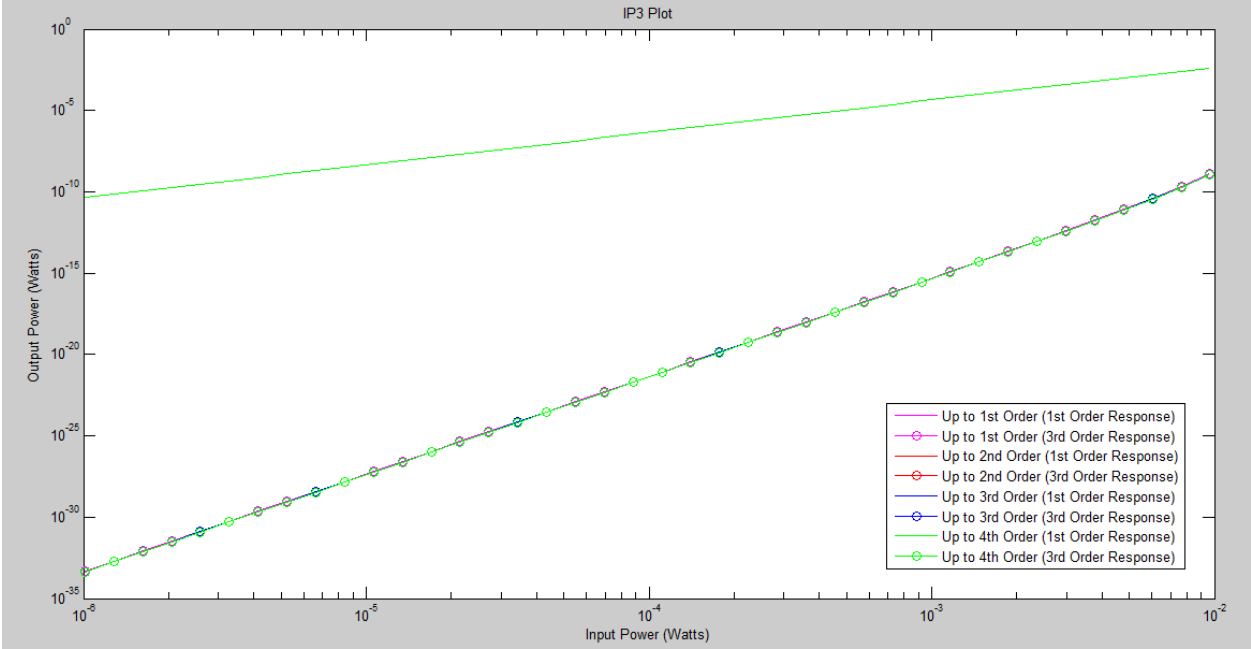

Figure 27: Top green curve: output power at a fundamental frequency. Lower curves: IMD3 for the first (magenta), second (red), third (blue), and fourth order (green) polynomial terms for the third order (-o) harmonic frequency responses.

The effect of nonlinearity on intermodulation distortion can be observed in the figure above. As expected, the output power has far larger spectral content at the fundamental frequencies than at the 3rd harmonic for average photocurrents below 10mA, and the UTC PD is essentially operating as a linear device. Above 40mA, a much larger fraction of the output power is diverted

from the fundamental frequencies into the harmonics, and the assumption of weak nonlinearity inherent in the harmonic balance method begins to break down. From Figure 27, IP3 can also be determined. The IP3 values for up to first, second, third, and fourth order polynomial terms are included below. Variations among these results are in the numerical noise.

Table 2. IP3 Values for Different Orders of Polynomial Terms Included At 100 MHz.

Order of Polynomial Terms Included	IP3
1	27.4297 dB
2	27.5119 dB
3	27.5119 dB
4	27.5378 dB

CHAPTER 5
ANALYZE AND MINIMIZE SOURCES OF NONLINEARITY

Intermodulation distortion in high-speed UTC photodiodes stems from the nonlinear variation of junction capacitance with both photocurrent and diode voltage. The former is directly related to optical input power, while the latter is influenced via feedback from an external circuit such as the bias tee (see Figure 25) considered in this thesis [1-3, 19-27].

The influence of heavy loading on diode voltage has a straightforward qualitative explanation, which is captured quantitatively in the model derived for this thesis. Consider the large-signal equivalent circuit of Figure 25. As photocurrent increases, so does the load current, and hence the voltage drop across the load resistance. Yet as the voltage drop across the load resistance increases, the voltage across the terminals of the UTC PD must decrease in order to satisfy Kirchoff's voltage law [40]. Lower diode voltage leads directly to an increase in junction capacitance [48-50].

The influence of optical illumination on junction capacitance is likewise straightforward to understand. When the optical illumination level is increased, the diode current is increased. Larger diode current means larger free electron density in the depletion region of the UTC PD. The larger free electron density in the depletion region of the UTC PD means a decrease in the net positive charge within the depletion region. With diode voltage held constant, however, the only way for Poisson's equation [42] to be satisfied with a lower net positive charge in the depletion region of the UTC PD is for the depletion region to increase in thickness. This increased thickness of the depletion region in turn leads to a decrease in junction capacitance [48-50].

More quantitatively, the voltage across the diode can be determined by the following

equation:

$$v_{diode} = v_{bi} + \int_{x_b}^{x_b+x_c} \frac{q}{\varepsilon}(N_D^- - n(x))dx \quad (69)$$

where v_{diode} is diode voltage, x_c is the depletion region width, ε is the permittivity of the depleted collector, N_D^- is the (weak) doping density in the depletion region, and n is the electron density generated by the optical illumination. Thus, when electron density generated by the optical illumination increases, the depletion region width also increases, with diode voltage held constant. This increase in depletion region width results in a decrease in junction capacitance due to the capacitance effect [48-50]. Similarly, with optical illumination power held constant, the electron density n(x) remains constant, and any decrease in diode voltage v_{diode} can only be accommodated by a commensurate decrease in depletion region thickness, x_c, and a commensurate increase in junction capacitance [48-50].

These two influences, heavy loading and the capacitance effects, will be offset at a certain diode voltage and cross-sectional area (A). Load resistance (R_L) will not be considered as a parameter for optimization, since it is constrained in most applications to approximately 50 Ω for purposes of efficient post-detection transimpedance amplification.

Therefore, the variation of the output power at the third order harmonic frequency ($2\omega_a - \omega_b$) as a function of applied voltage ($.1V$ to $100V$) and cross-sectional area ($1e-12\ m^2$ to $1e-6\ m^2$) has been calculated, and a corresponding surface plot generated in Figure 28 at a constant input photocurrent of 1mA. A zoomed-in version (1e-20W to 0W) is provided for convenience in Figure 29.

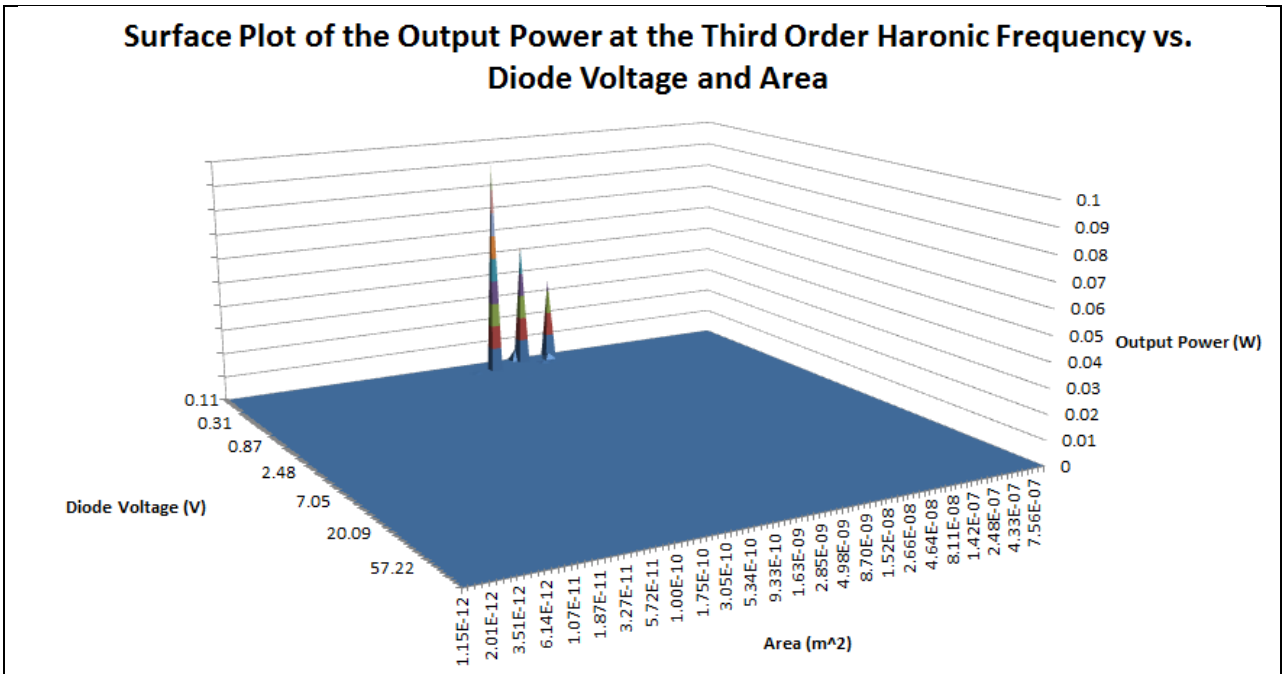

Figure 28: Surface plot of the output power at the third order harmonic frequency $(2\omega_a - \omega_b)$ versus diode voltage and cross-sectional area (A).

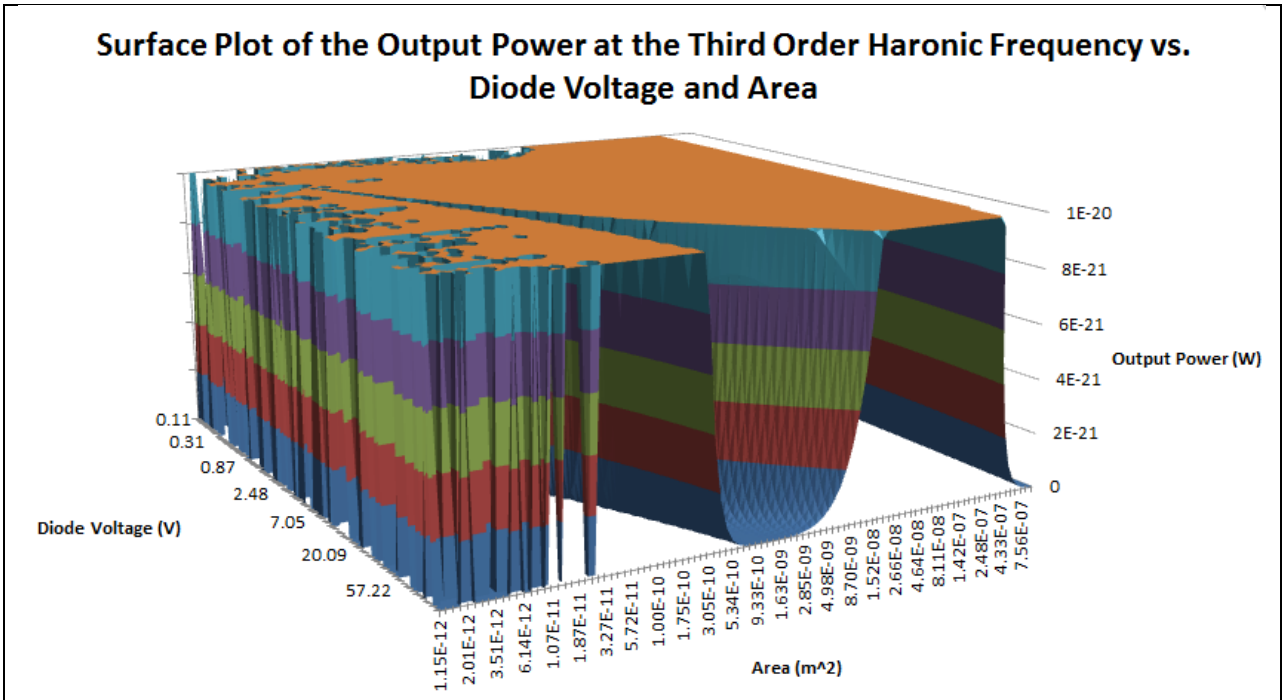

Figure 29: Surface plot of the output power at the third order harmonic frequency $(2\omega_a - \omega_b)$ versus diode voltage and cross-sectional area (A) (zoomed in).

As can be seen in the zoomed-in version of the surface plot, the two contributions to nonlinear capacitance, space charge screening and heavy loading, can be offset against each other to minimize IP3. Figure 28 quantifies the cross-sectional area of the UTC PD which is necessary the perfectly cancel capacitance-based intermodulation distortion for operation at a given diode voltage, such as $4.98e-11\ m^2$ at a diode voltage of $4.04\ V$ or $1.00e-10\ m^2$ at a diode voltage of $8.70\ V$.

CHAPTER 6
CONCLUSION

In this thesis, the weakly nonlinear operation of UTC PDs has been studied using physics-based equations expressing current continuity, electrostatic self-consistency, and coupling to an external circuit, and these equations have been cast in a phasor representation according to the method of harmonic balance [33]. This physics-based model involves three characteristic properties of the photodiode, one macroscopic and two microscopic: diode voltage (v_{diode}), the depletion region thickness (x_c), and the electric field at the beginning of the depletion region ($E(x_b)$). The model was then applied to a representative UTC PD device, and the magnitude of its intermodulation distortion IMD3 was calculated along with its 3rd order intercept point IP3, found to be approximately $27.5\ dB$, consistent with slight nonlinearity [12-18]. Finally, it was demonstrated that nonlinearity caused by the influences of space charge screening and heavy-loading effects on junction capacitance may be offset against each other, and a relationship between the UTC PD's cross-sectional area and junction voltage was quantified which theoretically eliminates intermodulation distortion [1-3].

REFERENCES

[1] V. J. Urick *et al.*, "Distortion in Fiber Optic Links," in *Fundamentals of Microwave Photonics*, Hoboken, NJ: John Wiley & Sons, Inc. 2015. [E-book] Available: Google e-book.

[2] E-G. Neumann, "Single Transmission Through Single-Mode Fiber," in *Single-Mode Fibers: Fundamentals*, Wuppertal, Fed. Rep. of Germany: Springer-Verlag Berlin Heidelberg, 1988. [E-book] Available: Google e-book.

[3] J. A. Nossek, "Circuits, Elements, Modeling, and Equation Formulation," in *Fundamentals of Circuits and Filters*, 3rd ed., W-K. Chen, Ed., Boca Raton, FL: CRC Press, 2009. [E-book] Available: Google e-book.

[4] T. Ishibashi *et al.*, "High-Speed Response of Uni-Traveling-Carrier Photodiodes," *Japanese Journal of Applied Physics*, vol. 36, pp. 6263-6268, 1997.

[5] H. Ito *et al.*, "High-Speed and High-Output InP–InGaAs Unitraveling-Carrier Photodiodes," *IEEE J. Sel. Topics. Quantum Electron*, vol. 10, no. 4, Aug.,pp. 709-727, 2004.

[6] T. Nagatsuma and H. Ito, "High-Power RF Uni-Traveling-Carrier Photodiodes (UTC-PDs) and Their Applications," in *Advances in Photodiodes*, G. F. D. Betta, ed., March 22, 2011. [E-book]. Available: Intech e-book.

[7] A. Wakatsuki *et al.*, "Development of Terahertz-wave Photomixer Module Using a Uni-traveling-carrier Photodiode," *NTT*, 2016. [Online]. Available: https://www.ntt-review.jp/archive/ntttechnical.php?contents=ntr201202fa5.html. [Accessed April 12, 2016].

[8] M. A. Khamsi and H. Knaust, "The Newton-Raphson Method," *sosmath.com*, 2015. [Online]. Available: http://www.sosmath.com/calculus/diff/der07/der07.html. [Accessed Dec. 21, 2015].

[9] A. Galantai, "The theory of Newton's method," in *Optimization and Nonlinear Equations*, L. T. Watson, M. Bartholomew-Biggs, and J. A. Ford, Eds., vol.4, Amsterdam, The Netherlands: Elsevier Science B. V., 2001. [E-book] Available: Google e-book.

[10] J. Bird, "Solving Equations by Iterative Methods," in *Engineering Mathematics*, 7th ed., New York, NY: Routledge, 2014. [E-book] Available: Google e-book.

[11] F. Cajori, "Euler, Lagrange, and Laplace," in *A History of Mathematics*, 5th ed., Providence, RI: AMS Chelsea Publishing, 2000. [E-book] Available: Google e-book.

[12] Y. Fu *et al.*, "Characterizing and Modeling Nonlinear Intermodulation Distortions in Modified Uni-Traveling Carrier Photodiodes," *IEEE J. of Quantum Electron.*, vol. 47, pp. 1312-1317, 2011.

[13] A. Oschlies *et al.*, "First-principles self-energy calculations of carrier-induced band-gap narrowing in silicon," *Physical Review B*, vol. 45, pp. 13741-13744, 1992.

[14] T. S. Moss, "Theory of Intensity Dependence of Refractive Index," *Physica Status Solidi B*, vol. 101, pp. 555-561, 2006.

[15] H. Pan *et al.*, "Characterization of high-linearity modified uni-traveling carrier photodiodes using three-tone and bias modulation techniques," *J. Lightw. Technol.*, vol. 28, pp. 1316-1322, 2011.

[16] H. Pan *et al.*, "The frequency behavior of the intermodulation distortions of modified uni-traveling carrier photodiodes based on modulated voltage measurements," *IEEE J. Quantum Electron.*, vol. 45, pp. 273-277, 2009.

[17] K. J. Williams and R. D. Esman, "Photodiode DC and microwave non-linearity at high currents due to carrier recombination nonlinearities," *IEEE Photonics Technol. Lett.*, vol. 10, pp. 1015-1017, 1998.

[18] D. Hall, "Understanding Intermodulation Distorion Measurements," *Electronic Design*, 2013. [Online]. Available: http://electronicdesign.com/communications/understanding-intermodulation-distortion-measurements. [Accessed April 12, 2016].

[19] I. Poole, "Photodiode Technology," *Radio-Electronics.com*. [Online]. Available: http://www.radio-electronics.com/info/data/semicond/photo_diode/photo_diode.php. [Accessed Dec. 21, 2015].

[20] APTechnologies, "Photodiode Theory of Operation," *www.aptechnologies.co.uk*, 2016. [Online]. Available: http://www.aptechnologies.co.uk/index.php/support/photodiodes/photodiode-theory-of-operation. [Accessed Dec. 21, 2015].

[21] Circuits TODAY, "Invention History of Phototransisor and Photodiode," *www.circuitstoday.com*, 2015. [Online]. Available: http://www.circuitstoday.com/invention-history-of-phototransistor-and-photodiode. [Accessed Dec. 21, 2015].

[22] D. Renker, "Geiger-mode avalanche photodiodes, history, properties and problems," In *Proc. 4th International Conference on New Developments in Photodetection*, vol. 567, no. 1, Nov., 2006, pp. 48-56.

[23] D. L. Morton, Jr. and J. Gabriel, "Imaging," in *Electronics: The Life Story of a Technology*, Baltimore, MD: The John Hopkins University Press, 2004. [E-book] Available: Google e-book.

[24] B. Woodward and E. B. Husson, "Photodiode Fundamentals," in *Fiber Optics Installer and Technician Guide*, Alameda, CA: SYBEX Inc., 2005. [E-book] Available: Google e-book.

[25] J. F. Cox, "Special Diodes," in *Fundamentals of Linear Electronics: Integrated and Discrete*, Albany, NY: Delmar, 2002. [E-book] Available: Google e-book.

[26] T. F. Schubert, Jr., and E. M. Kim, "Diode Characteristics and Circuits," in *Fundamentals of Electronics: Book 1: Electronic Devices and Circuit Applications*, Morgan & Claypool, 2014. [E-book] Available: Google e-book.

[27] T. Sir, "Semiconductor," *Physics365.com*, 2016. [Online]. Available: http://www.physics365.com/blog/?page_id=2284. [Accessed April 12, 2016].

[28] "P-I-N Photodiode | Avalanche Photo Diode," *electrical4u.com*, 2016. [Online]. Available: http://www.electrical4u.com/p-i-n-photodiode-avalanche-photo-diode/. [Accessed April 12, 2016].

[29] "Schottky barrier diode-construction-VI Characteristics-Applications," *ECE Tutorials: Electronics and control Systems*. [Online]. Available: http://ecetutorials.com/analog-electronics/schottky-barrier-diode/. [Accessed April 12, 2016].

[30] J. Pan, "Image sensor structure," U. S. Patent 09, 348,429, 22 Apr., 2003.

[31] M. Erman *et al.*, "Monolithic Integration of a GaInAs p-i-n Photodiode and an Optical Waveguide: Modeling and Realization Using Chloride Vapor Phase Epitaxy," *J. Lightw. Technol.*, vol. 6, no. 3, Mar., pp. 399-412, 1988.

[32] M. Nakano *et al.*, "$Mg_xZn_{1-x}O$-Based Schottky Photodiode for Highly Color-Sensitive Ultraviolet Light Detection," *Applied Physics Express*, vol. 1, no. 12, Dec., pp. 121201-1-121201-3, 2008.

[33] B. Troyanovsky *et al.*, "Physics-based simulation of nonlinear distortion in semiconductor devices using the harmonic balance method," *Comput. Methods in Appl. Mech. and Engrg.*, vol. 181, no. 4, pp. 467-482, Jan., 2000.

[34] A. S. Hastings *et al.*, "Minimizing Photodiode Nonlinearities by Compensating Voltage-Dependent Responsivity Effects," *J. Lightw. Technol.*, vol. 28, no. 22, pp. 3329-3333, Nov. 15, 2010.

[35] H. Pan *et al.*, "A High-Linearity Modified Uni-Traveling Carrier Photodiode With Offset

Effects of Nonlinear Capacitance," *J. Lightw. Technol.*, vol. 27, no. 20, pp. 4435-4439, Oct. 15, 2009.

[36] H. Pan *et al.*, "The Influence of Nonlinear Capacitance and Responsivity on the Linearity of a Modified Uni-Traveling Carrier Photodiode," In *Microwave photonics, 2008*, 2008, pp. 82-85.

[37] R. S. Quimby, "Avalanche Photodiode," *IHS Engineering 360*, 2016. [Online]. Available: http://www.globalspec.com/reference/21446/160210/chapter-14-4-1-avalanche-photodiode. [Accessed April 12, 2016].

[38] E. W. Weisstein, "Jacobian," *MathWorld.Wolfram.com*. [Online]. Available: http://mathworld.wolfram.com/Jacobian.html. [Accessed Dec. 21, 2015].

[39] B. V. Zeghbroek, "Continuity equation," in *Principles of Semiconductor Devices*, 2011. [Online]. Available: http://ecee.colorado.edu/~bart/book/book/chapter2/ch2_9.htm. [Accessed April 23, 2016].

[40] "Kirchoff's Circuit Law," 2016. [Online]. Available: http://www.electronics-tutorials.ws/dccircuits/dcp_4.html. [Accessed April 23, 2016].

[41] R. Nave, "Maxwell's Equations," *www.HyperPhysics.com*. [Online]. Available: http://hyperphysics.phy-astr.gsu.edu/hbase/electric/maxeq.html. [Accessed April 23, 2016].

[42] R. Nave, "LaPlace's and Poisson's Equations," *www.HyperPhysics.com*. [Online]. Available: http://hyperphysics.phy-astr.gsu.edu/hbase/electric/laplace.html. [Accessed April 23, 2016].

[43] A. Castoldi, "Signal formation in radiation detectors: Ramo's theorem and its application to practical cases," 2011. [Online]. Available: https://agenda.infn.it/getFile.py/access?contribId=28&sessionId=4&resId=0&materialId=slides&confId=3616. [Accessed April 23, 2016].

[44] E. W. Weisstein, "Taylor Series," *MathWorld.Wolfram.com*. [Online]. Available: http://mathworld.wolfram.com/TaylorSeries.html. [Accessed Dec. 21, 2015].

[45] G. M. Fikhtengol'ts, "Series of Numbers," in *The Fundamnetals of Mathematical Analysis: International Series of Monographs on Pure and Applied Mathematics*, vol. 2, Fitzroy Square, London: Pergamon Press Ltd., 1965. [E-book] Available: Google e-book.

[46] R. Shankar, "Mathematical Methods," in *Fundamentals of Physics: Mechanics, Relativity, and Thermodynamics*, Yale University, 2014. [E-book] Available: Google e-book.

[47] S. D. Promislow, "An Introduction to Stochastic Processes," in *Fundamentals of Actuarial Mathematics,* 3rd ed., West Sussex, United Kingdom: John Wiley & Sons, Ltd., 2015. [E-book] Available: Google e-book.

[48] R. Nave, "Capacitors," *www.HyperPhysics.com*. [Online]. Available: http://hyperphysics.phy-astr.gsu.edu/hbase/electric/capac.html. [Accessed Dec. 21, 2015].

[49] J. F. Becker, "Capacitors and Dielectrics (Insulators) – Chapter 24," in *Physics 51-Electricity & Magnetism*, 2009. [E-book] Available: San Jose State University e-book.

[50] B. V. Zeghbroek, "The p-n junction capacitance," in *Principles of Semiconductor Devices*, 2011. [Online]. Available: http://ecee.colorado.edu/~bart/book/pncap.htm. [Accessed Dec. 21, 2015].